Copy

COLLEGE OF ARTS AND SCIENCES

VIRGINIA POLYTECHNIC INSTITUTE AND STATE UNIVERSITY

Blacksburg, Virginia 24061

DEPARTMENT OF GEOLOGICAL SCIENCES 4044 DERRING HALL (703) 961-6521
Orogenic Studies

March 7, 1980

Dr. L. H. Brixner
Central Research and Development Dept.
E. I. Dupont deNemours & Co.
Wilmington, DE 19898

Dear Dr. Brixner:

Recently we have begun to attempt rare earth element analysis with the electron microprobe here at VPI, but are severely hindered by the lack of adequate standards. I work for a project studying potential geothermal resources in the southeastern USA. Because the area is geologically quiescent, we are looking at sites where the heat flow from the earth's interior is increased as a result of internal heat sources in the upper crust. These internal heat sources are the radioactive elements contained in the rocks in levels of less than 40 ppm. I am attempting to identify the mineral phases which contain the radioactive elements, and act as internal heat sources in the rocks, and their probable geologic behavior. I find that many of the uranium-and thorium-bearing minerals and minerals associated with them contain significant rare earth elements. Without microprobe standards there is little hope of characterizing these minerals in any detail.

In exploring possible ways to overcome the problem of microprobe standards, I ran across your paper on growing rare earth vanadates in the 1965 Journal of the Electrochemical Society, v 112. The technique of crystal growing appeared simple enough and an isomorphous series of end-member rare earth compounds would make ideal microprobe standards. I grew several grams of light-yellow, 0.1-0.5 mm $LaVO_4$ crystals, which are monoclinic. They are perfect for our needs, except that for many of the rare earths there is significant interference of the x-ray spectra with the vanadium spectra. I was wondering if there were other series of isomorphous rare earth element compounds which do not have interfering spectra, are stable in an electron beam, and that can be grown in a simple manner. Growing $LaVO_4$ are near my limit of crystal growing expertise.

If not or perhaps more simply, do you know of commercially available rare earth materials suitable for microprobe work? For the very small amounts of material needed, we can not justify having crystals specially grown. The metals and oxides are unsatisfactory because of their instability. Material grown for other purposes would be more than adequate. You utilized the electron microprobe in your paper on rare earth molybdates which appeared in the Handbook on the Physics and Chemistry of Rare Earths; what type of standards do you have for your own microprobe work? I would appreciate any help and insight you could provide in regard to rare earth element microprobe standards.

Sincerely yours,

J. Alexander Speer
Research Associate

JAS:mwd

ES-3178 REV. 1-75

DU PONT
REG. U.S. PAT. OFF.
ESTABLISHED 1802

E. I. DU PONT DE NEMOURS & COMPANY
INCORPORATED
WILMINGTON, DELAWARE 19898

CENTRAL RESEARCH & DEVELOPMENT DEPARTMENT
EXPERIMENTAL STATION

March 31, 1980

Dr. J. A. Speer
Virginia Polytechnic Institute and
State University
Department of Geological Sciences
4044 Derring Hall
Blacksburg, Virginia 24061

Dear Dr. Speer:

Thank you for your letter of March 7. I apologize for this delayed answer, but I only returned today from two weeks of vacation and business trips.

Regarding rare earth compound standards for your microprobe work, I could recommend the $Ln_2(MoO_4)_3$ type molybdates. These materials are indeed stable to the beam and single crystals where Ln = Pr, Nd, Sm, Ld, Dy, Ho and Er are available. If small pieces would do, I could send you these materials. I also have Ln doped $CaMoO_4$.

If you would like details on the microprobe work we did with these compounds, you would have to contact:

Mr. James Ficca
Micron, Inc.
Lancaster Ave and Center Rd.
Wilmington, DE

I hope this information will be of some help to you.

Sincerely yours,

L. H. Brixner

LHB/kac

Orogenic Studies Laboratory

April 8, 1980

Dr. L. H. Brixner
Experimental Station
Central Research & Development Dept.
E. I. duPont deNemours & Co.
Wilmington, Delaware 19898

Dear Dr. Brixner:

I would like to take advantage of your offer of the $Ln_2(MoO_4)_3$-type molybdates, Ln = Pr, Nd, Sm, Gd, Dy, Ho and Er, for microprobe standards. Fragments of 0.5-1mm^3 are more than adequate.for microprobe standards. However, from a practical standpoint, slightly larger pieces or several of the smaller fragments make mounting and polishing for quantitative analysis much easier.

If you would like to include Ln-doped $CaMoO_4$, I would be interested in determining detection limits of the rare earth elements. I assume the levels of the rare earth elements are low in the $CaMoO_4$; these would be good tests. For some other elements in ideal situations, limits of detection as low as 0.005 wt% have been possible. You would be welcome to use any of the results.

I appreciate your offer of the $Ln_2(MoO_4)_3$-type molybdates. These will allow us to begin work on how best to do quantitative analysis of rare earth elements with our automated system while preparing standards for the remaining elements. Work on the geologic materials can then begin that much sooner.

Sincerely yours,

J. Alexander Speer

JAS:mwd

ES-3178 REV. 1-75

DU PONT
REG. U.S. PAT. & TM. OFF.
ESTABLISHED 1802

E. I. DU PONT DE NEMOURS & COMPANY
INCORPORATED
WILMINGTON, DELAWARE 19898

CENTRAL RESEARCH & DEVELOPMENT DEPARTMENT
EXPERIMENTAL STATION

April 14, 1980

Dr. J. A. Speer
College of Arts and Sciences
Virginia Polytechnic Institute and
State University
Blacksburg, Virginia 24061

Dear Dr. Speer:

Thank you for your letter of April 8.

Under separate cover I am sending you the following single crystals:

1 - $GdDy(MoO_4)_3$
2 - $Gd_2(MoO_4)_3$
3 - $GdTb(MoO_4)_3$
4 - $Eu_2(MoO_4)_3$
5 - $Gd_2(W_{0.1}Mo_{0.9}O_4)_3$
6 - $Gd_{1.8}Er_{0.2}(MoO_4)_3$
7 - $Tb_2(MoO_4)_3$
8 - $SmGd(MoO_4)_3$
9 - $Nd_2(MoO_4)_3$
10 - $Pr_2(MoO_4)_3$ 1% Pr in Gd
11 - $Gd_{1.99}Nd_{0.01}(MoO_4)_3$
12 - $Sm_2(MoO_4)_3$
13 - $CaMoO_4$: 1% $NdNbO_4$
14 - $CaMoO_4$: 1% $SmNbO_4$

I trust that these will keep you busy for a while. Should you find 13 and 14 useful, I would have most of the other rare earth at the 1% level in $CaMoO_4$.

Best of luck.

Sincerely,

Lothar H. Brixner.

Lothar H. Brixner

LHB/dw

Y_2O_3	225.807
La_2O_3	325.817
Ce_2O_3	328.237
Pr_2O_3	329.811
Nd_2O_3	336.477
Pm	
Sm_2O_3	348.697
Eu_2O_3	351.917
Gd_2O_3	362.497
Tb_2O_3	365.845
Dy_2O_3	372.997
Ho_2O_3	377.857
Er_2O_3	382.517
Tm_2O_3	385.865
Yb_2O_3	394.077
Lu_2O_3	397.937

MoO_3 = 143.937

V_2O_5 = 181.879

WO_3 = 231.847

Nb_2O_5 = 265.807

SiO_2 = 60.084

Vanadates.

$LaVO_4$

La_2O_3	64.18
V_2O_5	35.82
	100.00

$YbVO_4$

Yb_2O_3	68.42
V_2O_5	31.58
	100.00

$TmVO_4$

Tm_2O_3	67.96
V_2O_5	32.04
	100.00

$LuVO_4$

Lu_2O_3	68.63
V_2O_5	31.37
	100.00

$Ln_2(MoO_4)_3$ - type molybdates.

#1 $GdDy(MoO_4)_3$

Gd_2O_3	22.67
Dy_2O_3	23.33
MoO_3	~~36.99~~ 54.01
	100.01

#2 $Gd_2(MoO_4)_3$

Gd_2O_3	45.64
MoO_3	54.36
	100.00

#3 $GdTb(MoO_4)_3$

Gd_2O_3	22.77
Tb_2O_3	22.98
MoO_4	54.25
	100.00

#4 $Eu_2(MoO_4)$

Eu_2O_3	44.90
MoO_4	55.10
	100.00

#5 $Gd_2(W_{0.1}Mo_{0.9}O_4)_3$

Gd_2O_3	44.17
WO_3	8.48
MoO_3	47.35
	100.00

#6 $Gd_{1.8}Er_{0.2}(MoO_4)_3$

Gd_2O_3	40.97
Er_2O_3	4.80
MoO_3	54.23
	100.00

#7 $Tb_2(MoO_4)_3$

Tb_2O_3	45.87
MoO_3	54.13
	100.00

#8 $SmGd(MoO_4)_3$

Sm_2O_3	22.14
Gd_2O_3	23.02
MoO_3	54.84
	100.00

#9 $Nd_2(MoO_4)_3$

Nd_2O_3	43.80
MoO_3	56.20
	100.00

#10 $Pr_2(MoO_4)_3$

Pr_2O_3	43.30
MoO_3	56.70
	100.00

#11 $Gd_{1.99}Nd_{0.01}(MoO_4)_3$

Gd_2O_3	45.42
Nd_2O_3	0.21
MoO_3	54.37
	100.00

#12 $Sm_2(MoO_4)_3$

Sm_2O_3	44.68
MoO_4	55.32
	100.00

#13 $CaMoO_4$: 1% $NdNbO_4$.

487.890 : 1% 602.284

493.913

CaO	11.35
MoO_3	87.43
Nd_2O_3	0.68
Nb_2O_5	0.54
	100.00

#14 $CaMoO_4$: 1% $SmNbO_4$

487.890 : 1% 614.504

494.035

CaO	11.35
MoO_3	87.40
Sm_2O_3	0.71
Nb_2O_5	0.54
	100.00

Handbook on the Physics and Chemistry of Rare Earths, edited by K.A. Gschneidner, Jr. and L. Eyring

Chapter 30

RARE EARTH MOLYBDATES (VI)

L.H. BRIXNER and J.R. BARKLEY
Central Research and Development Department, E.I. Dupont de Nemours & Co., Wilmington, Delaware 19898, USA

W. JEITSCHKO
Institut für Anorganische und Analytische Chemie, Justus-Liebig Universität, Giessen, F.R. Germany

Contents

Symbols

R = Rare earth atom
β = Phase of a particular structure type
Φ = Vacant A sites
α = Phase of a particular structure type
β' = Phase of a particular structure type
γ = Phase of a particular structure type
π = Amorphous phase
T_C = Curie temperature
P_s = Polarization
C^E_{ab} = Elastic constant
ω_M = Frequency
χ_{12} = Shear strain
χ_s = Spontaneous shear strain
E_0 = Threshold field
τ_0 = Critical threshold stress
d_{31} = Piezoelectric constant
k_3 = Electromechanical coupling coefficient
Δn_{ab} = Refractive index change
p_{ab} = Photoelastic constants
λ = Wavelength
μ_B = Magnetic moments
v = Wall velocity
μ_τ = Wall mobility
μ_E = Wall mobility
τ_0 = Threshold stress

1. Chemistry and crystal growth (L.H. Brixner)

1.1. *Introduction*

Although the rare earths as such, particularly in the form of their oxides, were known since as early as the late 18th century, it was not until over 100 years later when the first molybdates of these elements were described by Hitchcock (1895). Specifically he prepared such compounds as $Nd_2(MoO_4)_3$ or $Nd_2O_3{\cdot}3MoO_3$, which represents one of the more important stoichiometries of rare earth molybdates. Very few, if any, publications appeared in the literature thereafter until Borchardt and Bierstedt (1966) prepared certain members of the $R_2(MoO_4)_3$ series in the orthorhombic form and recognized they were ferroelectric. This finding sparked considerable interest in these compounds and practically all important preparative, structural and physical studies on the $R_2(MoO_4)_3$ compositions were conducted in the past ten years. In addition to the two most common types of rare earth molybdates, R_2MoO_6 and $R_2(MoO_4)_3$ (Megumi et al., 1974) described $R_2Mo_4O_{15}$ and $R_2Mo_6O_{21}$ compounds. The physical properties of these materials are less interesting and will only be discussed in context with the R_2O_3/MoO_3 phase equilibrium. In their phase diagram (Megumi et al., 1974) did not include the R_6MoO_6 composition, which was prepared by McCarthy (1974). Since this compound has a fluoride structure whose X-ray pattern closely resembles that of C-type Gd_2O_3, one can easily miss this composition on the Gd-rich side of the phase diagram. Finally, molybdates with the rare earth in unusual valence states such as the scheelite type $EuMoO_4$ with divalent europium were discribed by McCarthy (1971).

1.2. *The* R_2O_3-MoO_3 *phase diagram*

The phase equilibria are discussed for the Gd_2O_3/MoO_3 case according to Megumi et al. (1974). With 7f electrons, Gd represents the center of the rare earth series and should be fairly representative, although deviations due to changes in cohesive energy and ionic radius can be expected on either side of the Gd_2O_3/MoO_3 system.

Starting with the MoO_3 rich side, we first have the compound $Gd_2O_3{\cdot}6MoO_3$, whose structure is not known. The next compound is $Gd_2O_3{\cdot}4MoO_3$ which also has not yet been characterized structurally. This part of the phase diagram, from 0 to 25 mole% Gd_2O_3, is summarized in fig. 30.1. The balance of the phase diagram showing the $Gd_2O_3{\cdot}3MoO_3$ and $Gd_2O_3{\cdot}MoO_3$ phases is represented in fig. 30.2. As indicated in the previous section, the composition Gd_6MoO_6 should be added to complete the phase diagram.

One can see that this part of the phase diagram is considerably simpler than the MoO_3 rich side. It shows the two congruently melting compounds, $Gd_2O_3{\cdot}3MoO_3$ and $Gd_2O_3{\cdot}MoO_3$. Perhaps the most important feature established by Megumi et al. (1974) is the fact that there is essentially no phase width for $Gd_2O_3{\cdot}3MoO_3$ and only the precisely stoichiometric compound exists, a fact rather significant for single crystal growth.

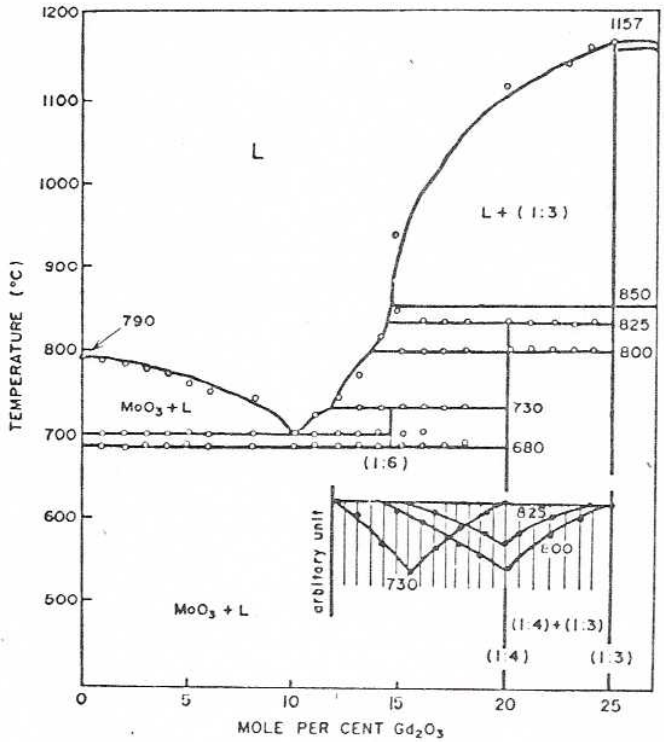

Fig. 30.1. Equilibrium diagram of the region 0–25 mole % Gd_2O_3: ○ DTA measured liquidus and solidus temperature, ● DTA halt maxima of the reactions at 730°C, 800°C and 825°C, plotted vs. composition.

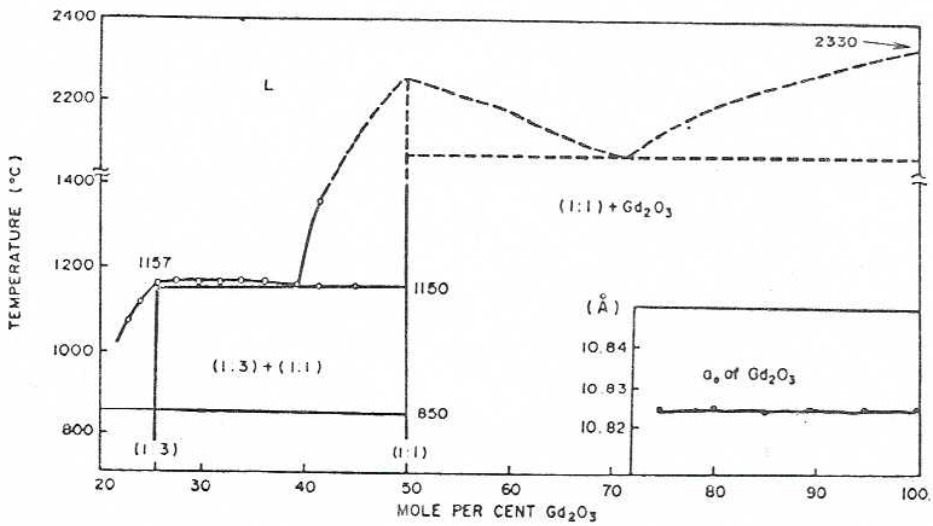

Fig. 30.2. High-temperature equilibrium diagram of the region 25–100 mole % Gd_2O_3: ○ DTA measured liquidus, ● lattice constants of Gd_2O_3 vs. composition.

TABLE 30.1.
X-ray diffraction data for $Gd_2O_3{\cdot}6MoO_3$ and $Gd_2O_3{\cdot}4MoO_3$.

$Gd_2O_3{\cdot}6MoO_3$		$Gd_2O_3{\cdot}4MoO_3$		$Gd_2O_3{\cdot}6MoO_3$		$Gd_2O_3{\cdot}4MoO_3$	
d(Å)	I	d(Å)	I	d(Å)	I	d(Å)	I
5.477	7	5.824	30	3.731	9	3.437	42
5.333	20	5.384	8	3.696	11	3.321	81
4.818	100	5.242	30	3.567	52	3.282	100
4.729	21	5.035	8	3.526	27	3.211	50
4.548	10	4.436	42	3.364	27	3.184	50
4.215	25	4.149	16	3.331	31	3.097	52
4.101	28	4.001	33	2.929	11	3.025	49
3.953	16	3.743	34	2.891	10	2.928	24
3.899	9	3.616	83	2.852	11	2.744	22
3.839	18	3.587	7	2.829	14	2.720	32

1.2.1. $Gd_2O_3{\cdot}6MoO_3$

Very little is known about this compound beyond the data given by Megumi et al. (1974). They did observe some single crystals in samples annealed at 720°C and then quenched to room temperature. Megumi et al. (1974) assume the structure to be orthorhombic and for identification purposes, their d-values are given in table 30.1.

1.2.2. $Gd_2O_3{\cdot}4MoO_3$

As with the previous compound, almost nothing is known about this composition. Its d-values are listed in table 30.1 together with $Gd_2O_3{\cdot}6MoO_3$.

1.2.3. $R_2O_3{\cdot}3MoO_3$

The molybdates of the rare earths formulated $R_2(MoO_4)_3$ are most important and are known for all R's as well as Y and Sc. They are discussed here in greatest detail. Because of the closely related electronic structures and the small variations in ionic size, most rare earth oxo-metallates such as the niobates $RNbO_4$ (Keller, 1962), the vanadates RVO_4 (Brixner and Abramson, 1965), the stannates $R_2Sn_2O_7$ (Whinfrey et al., 1960), and the titanates $R_2Ti_2O_7$ (Brixner, 1964) exhibit only one prototype structure at room temperature; however, the $R_2(MoO_4)_3$-type molybdates crystallize in four different structural arrangements. If one includes the temperature-dependent polymorphic modifications and thermodynamically metastable compositions, no less than eight different structures are known to exist for these compounds between room temperature and their respective melting points. This is indeed a fascinating body of rare earth compounds, unique in the protean display of structures as well as physical properties.

Starting with $La_2(MoO_4)_3$, we have two structures between the melting point and room temperature. When grown from the melt, the compound crystallizes in the space group $I4_1/a$ of an undistorted scheelite with the parameters listed in table 30.2. This structure can be frozen in, therefore suggesting that the phase transition at 848°C is sluggish and diffusion controlled. The fact that β-$La_2(MoO_4)_3$ crystallizes in a scheelite structure indicates that a better formulation for this compound might be $La_{2/3}\Phi_{1/3}MoO_4$ to show the relationship to the common ABO_4-type scheelite where A normally is a bivalent ion such as in $CaWO_4$.

Valence compensation in the lanthanum molybdate scheelite is achieved through $\frac{1}{3}$ vacancies in the A sites (indicated as Φ). In fact, it is the ordering of these

TABLE 30.2.

Lattice parameters, space groups, transition temperatures, and melting points of the $R_2(MoO_4)_3$-type rare earth molybdates.

R	Form	T(°C)	m.p.(°C)	a(Å)	b(Å)	c(Å)	β(deg)	Space group
La	α	848	–	17.006	11.952	16.093	108.44	C2/c
	β	–	1024	5.365	–	11.945	–	$I4_1/a$
Ce	–	None	1035	16.902	11.842	15.984	108.58	C2/c
Pr	α	987 to β	1045	16.849	11.778	15.914	108.50	C2/c
	β	–	–	7.444	–	10.901	–	$P\bar{4}_12m$
	β'	235 to β	–	10.526	10.578	10.901	–	Pba2
Nd	α	961 to β	1081	16.788	11.719	15.849	108.54	C2/c
	β	–	–	7.423	–	10.854	–	$P\bar{4}_12m$
	β'	225 to β	–	10.497	10.543	10.854	–	Pba2
Sm	α	910 to β	1122	7.562	11.509	11.557	108.98	C2/c
	β	–	–	7.380	–	10.769	–	$P\bar{4}2_1m$
	β'	197 to β	–	10.435	10.472	10.769	–	Pba2
Eu	α	881 to β	1144	7.554	11.459	11.497	109.08	C2/c
	β	–	–	7.363	–	10.727	–	$P\bar{4}2_1m$
	β'	180 to β	–	10.411	10.444	10.727	–	Pba2
Gd	α	857 to β	1171	7.575	11.436	11.424	109.28	C2/c
	β	–	–	7.347	–	10.701	–	$P\bar{4}2_1m$
	β'	159 to β	–	10.388	10.419	10.701	–	Pba2
Tb	α	835 to β	1172	7.529	11.379	11.401	109.21	C2/c
	β	–	–	7.321	–	10.653	–	$P\bar{4}2_1m$
	β'	160 yo β'	–	10.352	10.381	10.653	–	Pba2
Dy	α	805 to β	1222	7.514	11.344	11.364	109.31	C2/c
	β	1030 to γ	–	7.303	–	10.615	–	$P\bar{4}2_1m$
	β'	145 to β	–	10.327	10.351	10.615	–	Pba2
	γ	–	–	6.69	–	–	–	Cubic
Ho	β	853 to γ	1245	7.287	–	10.578	–	$P\bar{4}2_1m$
	β'	121 to β	–	10.304	10.324	10.578	–	Pba2
	γ	–	–	9.921	13.656	9.867	–	Pnca
Er	α	None	1320	9.936	13.515	9.827	–	Pnca
Tm	α	None	1390	9.909	13.445	9.782	–	Pnca
Yb	α	None	1421	9.864	13.411	9.759	–	Pnca
Lu	α	None	1445	9.828	13.389	9.734	–	Pnca

vacancies which is responsible for the structural transition into a monoclinic distortion at lower temperatures and we thus have an order–disorder transition at 848°C. For $Ce_2(MoO_4)_3$ the disordered scheelite was not observed, although we expect it to be thermodynamically stable at high temperature. Lattice parameters and melting point for $Ce_2(MoO_4)_3$ are also given in table 30.2. With $Pr_2(MoO_4)_3$, we begin the most interesting region of the rare earth molybdates not only because of the structural complexity but mainly because the next eight rare earth compounds (excluding Pm) exhibit the phenomena of ferroelectricity and ferroelasticity discussed in section 3.3. β-$Pr_2(MoO_4)_3$ melts congruently at 1045°C and has a phase transformation at 987°C. It is only within this narrow temperature range of 58°C that the tetragonal structure, space group $P\bar{4}2_1m$ is thermodynamically stable. However, the transformation is sluggish and diffusion controlled and therefore the high-temperature phase can be quenched in. As we can see in table 30.2 and fig. 30.3, this transformation temperature decreases as one proceeds to the smaller rare earth ions. Obviously the kinetics for the

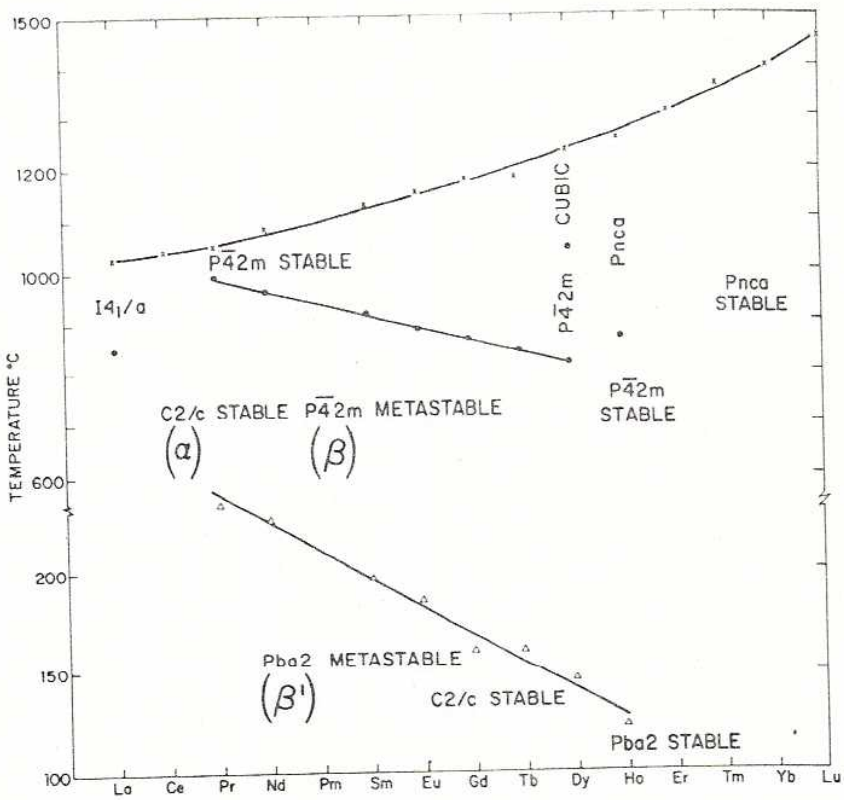

Fig. 30.3. Phase relationships of the $R_2(MoO_4)_3$-type rare earth molybdates.

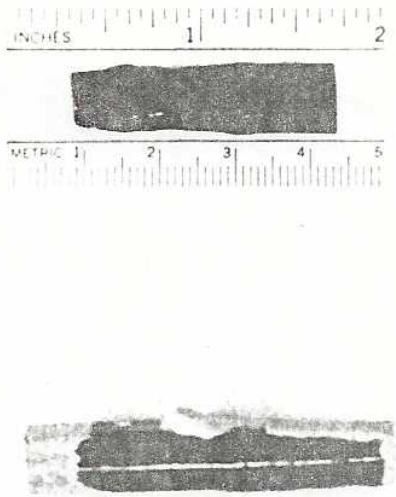

Fig. 30.4. $Nd_2(MoO_4)_3$ (top) and $Pr_2(MoO_4)_3$ crystals.

transformation to the thermodynamically stable low-temperature α structure are more favorable at the higher transformation temperature, and we believe that this is the reason why $Pr_2(MoO_4)_3$ and $Nd_2(MoO_4)_3$ have only recently been added to the list of ferroelectric rare earth molybdates by Brixner et al. (1971). To exemplify the difficulties with the α/β transformation for $Pr_2(MoO_4)_3$, we show in fig. 30.4 a typical crystal exhibiting some α phase despite rapid quenching. It is contrasted with a single crystal of $Nd_2(MoO_4)_3$ where the retention of essentially all β structure is possible. Structurally this noncentric $\bar{4}2m$ type is of great importance as it constitutes the parent phase from which all eight ferroelectric molybdates are derived. The high (β) and low (β') temperature phases of these structures are discussed in section 2. If the thermodynamically metastable β-$Pr_2(MoO_4)_3$ is further cooled below 987 to 225°C, it undergoes a second transformation leading to the lower symmetry ferroelastic-ferroelectric orthorhombic Pba2 structure. This structure is, of course, still thermodynamically metastable. Since it is derived from the high-temperature β structure, this type is designated as β'. This sequence of transformations from the stable high-temperature β structure to the metastable β and β' forms is the same for the next five rare earth ions and will therefore not be discussed again. The phase relationships with regard to temperature can best be seen in fig. 30.3. The reason for the increase in melting points of these compounds is the decrease in cell volume giving rise to increased cohesive energy. The thermodynamically stable, high-density, low-temperature α form of $Pr_2(MoO_4)_3$ is still isostructural with that of α-$La_2(MoO_4)_3$ which has already been discussed. Except for different melting and transformation temperatures, which can be obtained from fig. 30.3 and table 30.2, everything stated about $Pr_2(MoO_4)_3$ is

TABLE 30.3.
X-ray powder pattern for α-$Gd_2(MoO_4)_3$.

h	k	l	d_{obs}	d_{calc}	I_{obs}	I_{calc}	h	k	l	d_{obs}	d_{calc}	I_{obs}	I_{calc}
1	1	0	6.047	6.063	26	10	1	1	3	–	2.770	–	<1
1	2	−1		6.059		15	1	1	−4	–	2.768	–	<1
0	2	0	5.705	5.718	2	2	0	4	1	–	2.764	–	<1
0	0	2	5.384	5.391	19	22	2	2	1	2.723	2.726	8	6
0	2	1	5.045	5.052	18	16	2	2	−3		2.723		3
1	1	1	4.741	4.747	8	<1	0	0	4	–	2.696	–	<1
1	1	−2		4.742	–	1	1	3	2	2.673	2.673	7	5
0	2	2	–	3.923	–	1	1	3	−3		2.672		6
2	0	0	3.562	3.575	36	2	2	0	2	2.608	2.609	15	15
2	0	−2		3.572		6	2	0	−4	2.605	2.605	14	15
1	1	2		3.564		17	0	4	−2	2.526	2.526	3	3
1	1	−3		3.560		17	3	1	−1	2.447	2.450	1	1
1	3	0	3.361	3.364	5	5	3	1	−2		2.449		<1
1	3	−1		3.363		1	0	2	4	–	2.438	–	<1
2	2	−1	3.158	3.158	100	100	2	2	2	–	2.374	–	<1
1	3	1	3.074	3.070	7	<1	2	2	−4	–	2.371	–	<1
1	3	−2		3.077		<1	3	1	0	2.333	2.333	2	1
0	2	3	3.043	3.043	84	79	3	1	−3		2.331		<1
2	2	0	–	3.031	–	<1	1	3	3	2.281	2.285	2	<1
2	2	−2	–	3.029	–	<1	1	3	−4		2.284		<1
0	4	0	2.858	2.859	27	27	2	4	−1		2.282		<1

true also for $Nd_2(MoO_4)_3$. While the high-temperature structure stays the same for $Sm_2(MoO_4)_3$, we now have a new structure for the α form. This phase is isostructural with $Eu_2(Wo_4)_3$ for which the complete structure has been determined by Templeton and Zalkin (1963). To demonstrate this relationship, intensity calculations were carried out for α-$Gd_2(MoO_4)_3$ using the published positional parameters of $Eu_2(WO_4)_3$. The good agreement between the calculated intensities and the powder intensities is indicated in table 30.3. The density of α-$Sm_2(MoO_4)_3$ is 5.450 g/ml^{-1} and that of β'-$Sm_2(MoO_4)_3$ is 4.405 g/ml^{-1}. This density difference is unusually large, reaching almost 25%. It suggests that the β'-structure is rather open and the application of pressure may cause it to collapse. A pressure experiment showed that the $\beta \rightarrow \alpha$ transformation for $Gd_2(MoO_4)_3$ occurs some 300°C below the ambient transformation point of 855°C. Application of higher pressures and lower temperatures finally led to yet another structural modification called π-GMO[$Gd_2(MoO_4)_3$]. This form of $Gd_2(MoO_4)_3$ is amorphous, and experimental details have been given by Brixner (1972). The β' structure collapses under the influence of high pressure, but a complete structural rearrangement is impossible because of the slow kinetics at room temperature resulting in an amorphous structural disarray intermediate between the α and β' structures. The effect of hydrostatic pressure on the β'/β phase transition has been studied by Shirokov et al. (1972). These authors find that as little as 3 kbar raise the Curie temperature from 160°C to almost 240°C.

TABLE 30.4.
X-ray diffraction data for Gd_2O_3·3MoO_3.

I	d(Å)	I	d(Å)
30	10.699	100	3.478
60	6.059	100	3.293
80	5.349	100	3.284
20	5.207	30	3.209
90	4.679	100	3.031
20	4.326	95	2.941
5	4.269	90	2.804
100	3.729	80	2.799
100	3.677	20	2.674
90	3.566		

I_{obs}	I_{calc}
–	<1
–	<1
–	<1
8	6 3
–	<1
7	5 6
15	15
14	15
3	3
1	1 <1
–	<1
–	<1
–	<1
2	1 <1
2	<1 <1 <1

...s the same
...his phase is
been deter-
...tionship, in-
...e published
...e calculated
...e density of
g/ml^{-1}. This
ests that the
cause it to
...rmation for
on point of
...ly led to yet
...is form of
...n by Brixner
ssure, but a
...w kinetics at
intermediate
on the β'/β
authors find
lmost 240°C.

In connection with this change of transition temperature via pressure, it is also interesting to refer to the work by Dem'yanov and Shchedrin (1973) who found that neutron irradiation can raise the β'/β phase transition by as much as 200 K permanently. $Eu_2(MoO_4)_3$, $Gd_2(MoO_4)_3$ and $Tb_2(MoO_4)_3$ exhibit exactly the same structural transformations as did $Sm_2(MoO_4)_3$ and detailed numbers can again be extracted from table 30.2 and fig. 30.3. For purposes of identification, the first 19 lines of the β'-$Gd_2(MoO_4)_3$ X-ray diagram are given in table 30.4. Recently, Naussau et al. (1971) mentioned yet another structural modification of Eu, Gd, Tb and Dy-molybdate called γ-phase. We have also observed such a phase for $Tb_2(MoO_4)_3$ but obtained it only upon crystallization from a super-cooled melt and never upon heating of the β phase to the melting point. We therefore believe this to be yet another metastable phase. It appears to be of cubic symmetry. If one looks at the phase relationship diagram in fig. 30.3 and the lattice parameters in table 30.2, it would appear that $Dy_2(MoO_4)_3$ is the easiest compound to grow since its β/α transformation is the lowest and its orthorhombic distortion ($b - a$) the least. And yet $Dy_2(MoO_4)_3$ cannot be obtained as a sound single crystalline boule at all. The reason for this is yet another phase transformation at 1030°C which is disruptive. This means that the volume change associated with the structural transition is so large that the boule will invariably break up. We succeeded in freezing in this δ-phase and tentatively identified it as cubic with a cell edge of 6.96 Å. After this experience, we set out to establish the material which exhibits the lowest β/α transformation and the least $b - a$ distortion which can be grown without this disruptive phase transition. This information is summarized in table 30.5. One can see that as little as 3 Å^3 in cell size or 0.001 Å difference in ionic radius determines whether a transition occurs or not. Although not precisely at this transition point, the compound $GdDy(MoO_4)_3$ does grow with greatest ease and has been obtained free of any α phase and thus not exhibiting any laser light scattering. Such a crystal is shown in figs. 30.5 and 30.6. $Ho_2(MoO_4)_3$ constitutes yet another special case. Contrary to Nassau (1971), we were unable to produce an α phase of

TABLE 30.5.
Lattice parameters and β/δ transition temperature for some Pba2-type solid solutions.

Composition	a(Å)	b(Å)	c(Å)	V(Å)	IR(Å)	$T_{\beta/\delta}$ (°C)	Sound boule
$Dy_2(MoO_4)_3$	10.3271	10.3513	10.6145	1134.68	0.912	1030	No
$DyTb(MoO_4)_3$	10.3374	10.3631	10.6339	1139.18	0.918	1114	No
$Dy_{1.4}Gd_{0.6}(MoO_4)_3$	10.3377	10.3628	10.6303	1138.79	0.920	1143	No
$Dy_{0.4}Tb_{1.6}(MoO_4)_3$	10.3457	10.3738	10.6460	1142.57	0.921	No	Yes
$Dy_{1.2}Gd_{0.8}(MoO_4)_3$	10.3490	10.3749	10.6433	1142.78	0.922	No	Yes
$DyGd(MoO_4)_3$	10.3582	10.3837	10.6564	1146.16	0.925	No	Yes

$Ho_2(MoO_4)_3$ at all, and we believe the β' and β structures to be the only thermodynamically stable ones of all the ferroelectric rare earth molybdates. But a new structural complication enters the picture: γ-$Ho_2(MoO_4)_3$. This structure is orthorhombic, space group Pnca and has been determined by Abrahams (1966) for $Sc_2(WO_4)_3$. The transition from β to γ-$Ho_2(MoO_4)_3$ at 853°C is again disruptive, and no sound boules of β or β'-$Ho_2(MoO_4)_3$ can be obtained. In addition to this problem, $Ho_2(MoO_4)_3$ tends to hydrate at room temperature causing further difficulties. The remaining rare earth molybdates of Er, Tm, Yb and Lu also form hydrates and crystallize only in the Pnca structure without any phase transitions. We have determined their cell dimensions but only in the case of $Lu_2(MoO_4)_3$ was this done on a pure single crystal which gave no additional diffraction lines outside the Pnca structure. The other compounds did contain small quantities of the hydrate, and the lattice parameters therefore have to be taken with some reservations. The cell volumes as a function of the best reported ionic radii by Shannon and Prewitt (1969) for the ferroelectric Pba2 compositions are shown in fig. 30.7. In order to get a perfect straight-line relationship, the ionic radius for Pr^{+3} in eight-fold coordination had to be corrected from 0.997 to 0.991 Å.

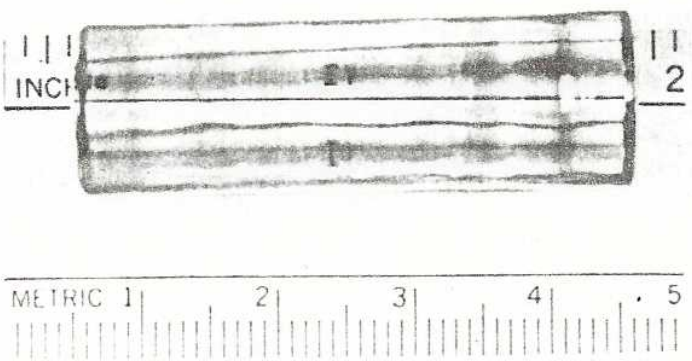

Fig. 30.5. $GdDy(MoO_4)_3$ single crystal viewed sideways.

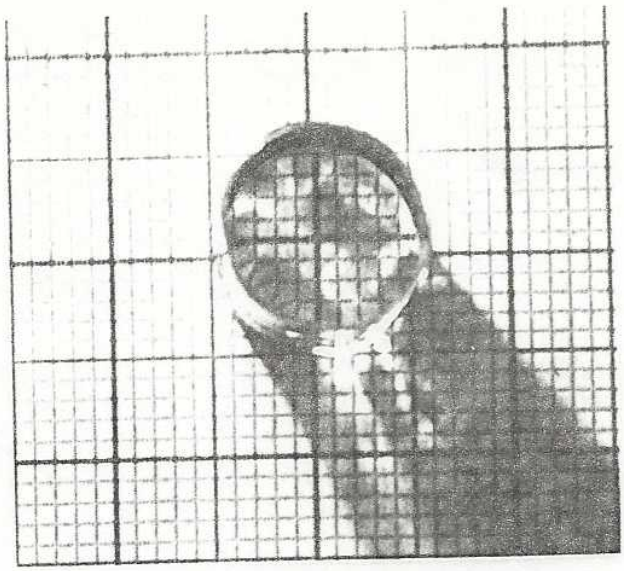

Fig. 30.6. $GdDy(MoO_4)_3$ single crystal viewed along growth axis.

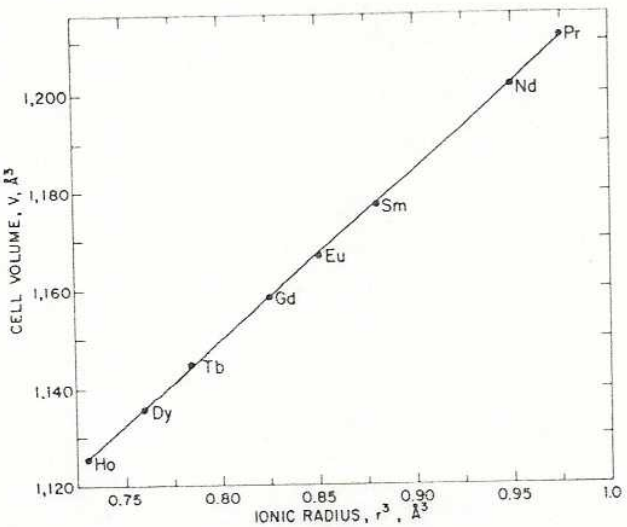

Fig. 30.7. r^3 vs. cell volume for the ferroelectric β'-type $R_2(MoO_4)_3$ molybdates.

1.2.3.1. *Single crystal growth of* $R_2O_3{\cdot}3MoO_3$ *compounds*

Since other species, such as, for instance, the Ln_2MoO_6 compounds exist in the Ln_2O_3–MoO_3 phase diagram, extreme care must be taken in preparing feed material of high purity and precise stoichiometry. In a solid state reaction where one component sublimes at 770°C and the other melts above 2000°C, this is not easy. The constituent components were the rare earth oxides of at least 99.99% purity obtained from the Kerr-McGee Company, and Climax Molybdenum Co. Ammonium molybdate $(NH_4)_6Mo_7O_{24}{\cdot}4H_2O$ was used as a precursor for high purity MoO_3. The rare earth oxides were fired at 1000°C in air or oxygen for at least 5 to 8 h to ensure the removal of all volatile matter such as H_2O, CO_2, etc. They were subsequently kept in the desiccator. MoO_3 was prepared by first heating the ammonium salt to 300°C for 10 to 14 h, subsequently raising the temperature to 600°C for another 10 to 14 h. This procedure yielded a highly crystalline pale-yellow MoO_3. The constituent components were weighed to the nearest mg, mixed for at least 30 min on a "WIG-L-BUG", and fired at 600°C for 10–14 h. After the mixture was ground and refired 1 to 2 h at 600°C, the temperature was raised to 900°C for 2–4 h. Any weight loss occurring during the firing operations was carefully made up with MoO_3. All colorless rare earth oxides yielded pure-white powders of the corresponding molybdates.

Single crystals were grown by the Czochralski technique, using a 20 kVA "Ecco" high frequency generator as a power source. The working coil was 3 inch OD 8 turns fabricated from flattened $\frac{1}{4}$ inch Cu tubing. The crucible was of 60 mil thick iridium $1\frac{1}{2}$ inch high and $1\frac{1}{2}$ inch wide. Typical growth rates for approximately $\frac{1}{2}$ inch diameter crystals were 0.5 to 0.8 cm/h. Seed rotational speeds varied from 80 to 120 rpm.

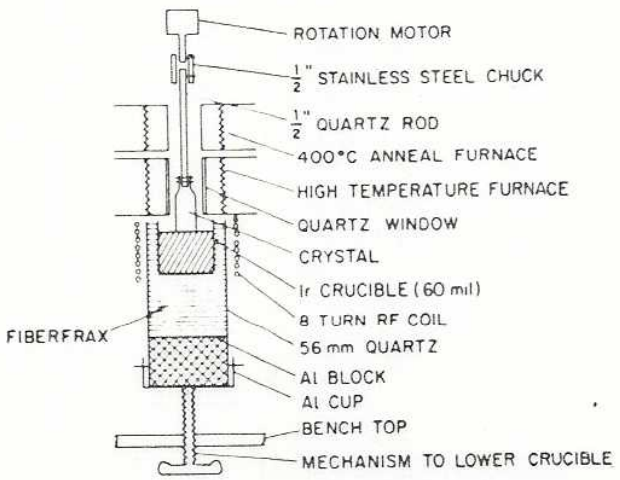

Fig. 30.8. Set-up for Czochralski growth of $R_2(MoO_4)_3$ single crystals.

A problem commonly encountered during growth of these crystals is expansion of the melt upon freezing, which severely distorts the container and often renders it useless after only a few runs. This can be greatly minimized by providing a mechanism which permits the melt to directionally freeze at the end of a run. As can be seen in fig. 30.8, a feed screw lowers the crucible in such a position that the top of the melt is hot while the bottom freezes. There is still slight bulging towards the sides but as many as 50 crystal growth runs could be carried out in the same container without excessive distortion of the crucible if this was done. Repeated melting and freezing during the initial charging of the container is also eliminated if a large quartz funnel is used to continuously feed the powder to the melt until the proper level is obtained. As some of the high-temperature structures (e.g. Pr and Nd) are only stable in a very narrow temperature range, crystal growth had to be carried out in the presence of an afterheater held at the right temperature. This is schematically shown in fig. 30.8. The purpose of the second heater is to allow rapid quenching of the crystal to about 400°C and slow cooling from there. $Lu_2(MoO_4)_3$ melted at approximately 1450°C and crystal growth was carried out under 200 psi argon pressure. This greatly reduced but did not eliminate completely the significant vaporization of MoO_3 observed under ambient conditions. MoO_3 losses start becoming noticeable with the Ho compound.

$Gd_2(MoO_4)_3$ was most extensively studied. With a melting point of 1171°C and a β/α transformation temperature of 857°C, we have a reasonably broad stability range of 314°C and $Gd_2O_3{\cdot}3MoO_3$ crystals can be grown without an afterheater. However, such crystals will contain small uniformly distributed quantities of α phase giving rise to strong nonspecular scatter of a laser beam passed through the crystal. This type of defect was termed "dispersed inclusions" by Borchardt (1968). Another serious problem, called "axial inclusions" or "feathers" by Borchardt (1968) has also been quantitatively characterized. These defects are Gd_2MoO_6 as first evidenced by a microprobe traverse across such an inclusion. The relative shifts of the Gd and Mo concentrations come close to the calculated amounts for the differences in $Gd_2(MoO_4)_3$ and Gd_2MoO_6. Later on we also succeeded in characterizing this inclusion by X-rays as Gd_2MoO_6. Its elimination requires the establishment of a flat temperature profile at the crystal/liquid interface. This is achievable in the range of 80 to 120 rpm rotation of the crystal. One other problem is inclusion of metallic particles giving rise to strong specular scatter of a laser beam passed through the crystal. This is observed when either Pt or Pt/Rh containers are used. Epstein (1970) did observe such inclusions and assumed them to be Pt. An electron microprobe analysis of a thin single crystalline slice containing such particles clearly characterized them as metallic Pt as can be seen in fig. 30.9. The use of Ir containers eliminates this problem as neither Ir nor IrO_2 appears soluble in detectable quantities in the melt. We have grown $Gd_2(MoO_4)_3$ on [100], [001] and [110] oriented seeds, obtaining the best results with the latter orientation. This is probably due to the fact that the domain walls entering the crystal on cooling through the Curie temperature at 159°C come in along the boule axis, thereby causing the least amount of stress which can give rise to cracking of boules.

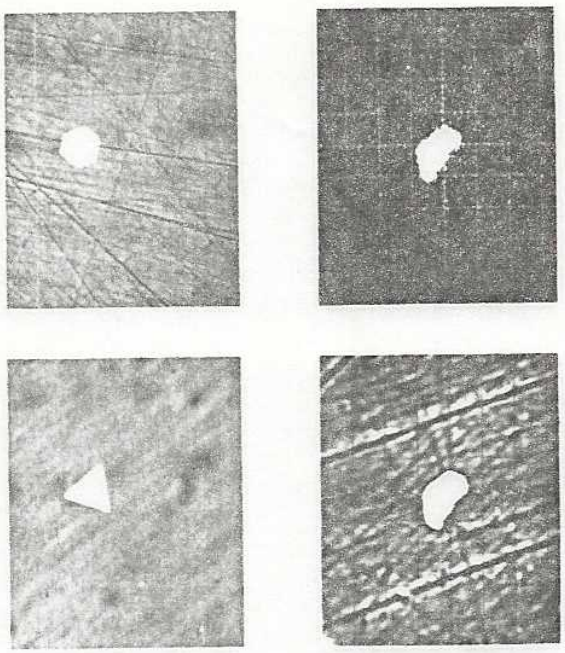

Fig. 30.9. Pt inclusions in $Gd_2(MoO_4)_3$. Left: optical micrographs. Right: top, Pt electron image; bottom: Pt X-ray image.

Combining all this information for the growth of high quality $Gd_2(MoO_4)_3$, the following is suggested.

(1) Prepare quality feed from high purity constituent components. For ultra-high quality, it will further help to use previously grown and thereby purified material.

(2) Grow on [110] seed from $1\frac{1}{2}$" diameter Ir pot at speeds not exceeding 0.8 cm/h and a rotation rate of the crystal of 100 rpm.

(3) Keep crystal diameter under $\frac{1}{2}$ inch and above β/α transition throughout growth process; subsequently quench rapidly to 400°C.

(4) Cool at 40°C/h or less with a slight temperature gradient from top to bottom of crystals, so walls will enter in the same way.

1.2.4. *The* R_2O_3-MoO_3 *compounds*

As became apparent through the discussion of the metastability of the ferroelectric parent phase, crystal growth of these materials does pose very specific problems. In addition to the possible inclusion of α phase, one must also be concerned about precise stoichiometry. Specific problems are the R_2MoO_6-type compounds which are related to the previously discussed materials via the equation

$$R_2(MoO_3)_3 \rightarrow R_2MoO_6 + 2MoO_3$$

The first R_2MeO_6-type compound where Me = W and R = Yb was probably synthesized by Cleve (1902) and the first molybdate (La_2MoO_6) by Sillen (1943).

According to Sillen (1943), the structure of La_2MoO_6 can best be described as consisting of La_2O_2 and MoO_4 layers. An La_2O_2 layer has in its center a flat square oxygen network in whose interstices the La ions alternately occupy one or the other side. Thus, it is the same arrangement which has been reported for oxyhalides such as LaOCl and LaOBr. The space group is $I\bar{4}2m$, constituting noncentric symmetry similar to the β structure of the ferroelectric $R_2(MoO_4)_3$ compounds. Ce_2MoO_6, first reported by Brixner et al. (1972), constitutes an exception in the series of tetragonal R_2MoO_6 compounds. We chose to prepare it by a symproportionation according to

$$6CeO_2 + Mo + 2MoO_3 \rightarrow 3Ce_2MoO_6$$

in sealed quartz ampoules. The compound is black, semiconducting, and of different structure than La_2MoO_6. It crystallizes in a cubic symmetry similar to CaF_2, suggesting that all R_2MoO_6 compounds may be derived from this prototype by way of ordering and distortion with the three metal ions distributed over the Ca sites and the oxygens in the F position. The fact that Ce_2MoO_6 is the only R_2MoO_6-type molybdate which is not an insulator suggests that one has a distribution of variable valence states for the Ce ions and pentavalent Mo such as in $Ce^{+3}Ce^{+4}Mo^{+5}O_6$. Pr_2MoO_6 crystallizes in $I\bar{4}2m$ symmetry, and its parameters are listed in table 30.6. This same structure was obtained for Nd_2MoO_6 and Sm_2MoO_6. The latter compound could also be obtained in a monoclinic form, if prepared at low temperatures. This brings us to the new structure of all remaining rare earth molybdates of the type R_2MoO_6, starting with Eu_2MoO_6. Blasse (1966) had given a suggested cell for these compounds

TABLE 30.6.
Lattice parameters and space groups for the Ln_2MoO_6 compounds.

Ln	a(Å)	b(Å)	c(Å)	β(deg)	Space group
La	4.093	–	16.017	–	$I\bar{4}2m$
Ce	5.578	–	–	–	$Fm3m$*
Pr	4.030	–	15.852	–	$I\bar{4}2m$
Nd	4.005	–	15.813	–	$I\bar{4}2m$
Sm	3.965	–	15.686	–	$I\bar{4}2m$
	16.628	15.791	5.470	108.28	C2/c
Eu	16.558	15.735	5.439	108.16	C2/c
Gd	16.514	15.678	5.425	108.33	C2/c
Tb	16.462	15.626	5.396	108.35	C2/c
Dy	16.542	15.573	5.371	109.72	C2/c
Ho	16.469	15.516	5.349	109.60	C2/c
Er	16.412	15.479	5.328	109.53	C2/c
Tm	16.266	15.419	5.310	108.57	C2/c
Yb	16.240	15.387	5.290	108.66	C2/c
Lu	16.211	15.346	5.274	108.80	C2/c

*Subcell?

based on a distortion of Sillen's tetragonal La_2MoO_6. The data were not based on single crystals, and we were completely unable to index our Guinier data using Blasse's (1966) parameters. We therefore attempted to grow single crystals of Gd_2MoO_6 even though the compound melts near 2000°C. We were able to obtain single crystals of a Bi-substituted Gd molybdate of the type $Ge_{1.7}Bi_{0.3}MoO_6$. This allowed us to establish the space group C2/c (Cc was ruled out by a negative second harmonic generation test) with $a = 16.62$ Å, $b = 11.23$ Å, $c = 5.45$ Å and $\beta = 108.6°$. One can also use a body-centered cell to describe this structure. There is an obvious relationship to the tetragonal cell of the large rare earth molybdates:

$$a_M \sim \sqrt{2} \times a_T, \qquad b_M \sim \sqrt{2} \times a_T, \qquad c_M \sim c_T.$$

Sm_2MoO_6 is the link between these two structures as it was obtained in both forms. The transition from tetragonal to monoclinic is not merely a distortion because the tetragonal form is readily obtained at room temperature by air quenching. Thus the transition is slow and involves some rearrangement of atoms. The monoclinic modifications are denser, and high pressure should convert the tetragonal to the monoclinic form. This was possible at 65 kbar with Nd_2MoO_6, although the indexing of the film was not perfect. The parameters for Gd_2MoO_6 are listed in table 30.6. For the remaining R_2MoO_6-type rare earth molybdates, the structural situation is simple as they all crystallize in the C2/c type. Parameters for Tb_2MoO_6, Dy_2MoO_6, Ho_2MoO_6, Er_2MoO_6, Tm_2MoO_6, Yb_2MoO_6 and Lu_2MoO_6 are listed in table 30.6. Compared to the complexity of structures for the $R_2(MoO_4)_3$ compounds, we certainly have a more "normal" situation with regard to structural types for these R_2MoO_6 compositions.

2. Crystal chemistry, phase transitions, and crystallographic aspects (W. Jeitschko)

The crystal structures of most compounds treated in the previous section are known. They will be discussed and compared here with the emphasis on the differences among the individual structural types. The structural and crystallographic aspects of the displacive phase transition between β and β'-$Gd_2(MoO_4)_3$ will be treated in more detail, since they are the basis for the interesting physical properties to be discussed in the final section.

2.1. *Composition* $R_2(MoO_4)_3$

The crystal structures of this composition belong to three basically different structural families with a total of six well characterized structural types: a) defect scheelite structures which can be disordered (1), or ordered of $La_2(MoO_4)_3$ type (2) or $Eu_2(WO_4)_3$ type (3); b) β-$Gd_2(MoO_4)_3$ above (4) and below (5) its displacive phase transition; and c) the $Sc_2(WO_4)_3$ type (6) structure. For γ-$Dy_2(MoO_4)_3$ a seventh structure was tentatively identified by Brixner (1973) as

cubic. Finally amorphous π-$Gd_2(MoO_4)_3$ obtained by "crushing" β-$Gd_2(MoO_4)_3$ under high pressure can be counted as an eight modification.

The main differences of the three structural families are in the oxygen coordination of the R ions which decreases from eight in the defect scheelites, over seven in β- and β'-$Gd_2(MoO_4)_3$ to six in the $Sc_2(WO_4)_3$ type compounds. The Mo atom is always tetrahedrally coordinated by oxygen although octahedral coordination of Mo is known for other compositions.

2.1.1. *Defect scheelites* $R_2(MoO_4)_3$

The $La_2(MoO_4)_3$ type structure (Jeitschko, 1973) which occurs for R = La, Ce, Pr, Nd, and the $Eu_2(WO_4)_3$ type structure (Templeton and Zalkin, 1963) found for the molybdates with R = Sm, Eu, Gd, Tb, Dy, are best described as derived from scheelite, $CaWO_4$. The formula $R_2(MoO_4)_3$ can be expressed as $R_{2/3}\phi_{1/3}MoO_4$ where ϕ stands for vacant sites. The ordered arrangement of vacancies and R atoms on the Ca site of scheelite gives rise to the superstructures which are shown in fig. 30.10. The main differences between the $La_2(MoO_4)_3$ and the $Eu_2(WO_4)_3$ type structure is the arrangement of the R atoms and the vacancies. Atomic positions in $La_2(MoO_4)_3$ deviate only little from those in scheelite. Considerable distortions from an ideal scheelite arrangement occur in $Eu_2(WO_4)_3$. They may, however, be due to the tendency of W for higher coordination (for compositions which occur for both, molybdates and tungstates, it is sometimes observed that W is in octahedral and Mo in tetrahedral coordination) and therefore the distortions may not be present in a molybdate with $Eu_2(WO_4)_3$ type structure. To answer the question of why the $La_2(MoO_4)_3$ type structure occurs for the big R elements and the $Eu_2(WO_4)_3$ type structure for the smaller ones, an accurate structure refinement for a $R_2(MoO_4)_3$ compound with $Eu_2(WO_4)_3$ type structure would be needed.

Compounds with a superstructure due to an ordering process usually have an order–disorder transition at higher temperatures. As discussed above, such a transition was found for $La_2(MoO_4)_3$ about 200°C below the melting point. In $Ce_2(MoO_4)_3$ this transition was not observed probably because of insufficient quenching. In the remaining $R_2(MoO_4)_3$ compounds the defect scheelite structure is thermodynamically not stable at all at high temperatures and therefore the order-disorder transition does not need to occur. The relatively high speed of the order–disorder transition in $La_2(MoO_4)_3$ is easily rationalized since the La positions and vacant sites are interconnected and furthermore at high temperatures the MoO_4 tetrahedra can be easily displaced from their ideal positions.

2.1.2. β- *and* β'-$Gd_2(MoO_4)_3$

The primary cristallization product of $R_2(MoO_4)_3$ compounds (R = Pr to Ho) has the β-$Gd_2(MoO_4)_3$ type structure. As discussed above, this structure becomes thermodynamically metastable for most compositions a few hundred °C below the melting point. Nevertheless it is kinetically very stable at lower temperatures and undergoes a displacive phase transition to the ferroelastic-

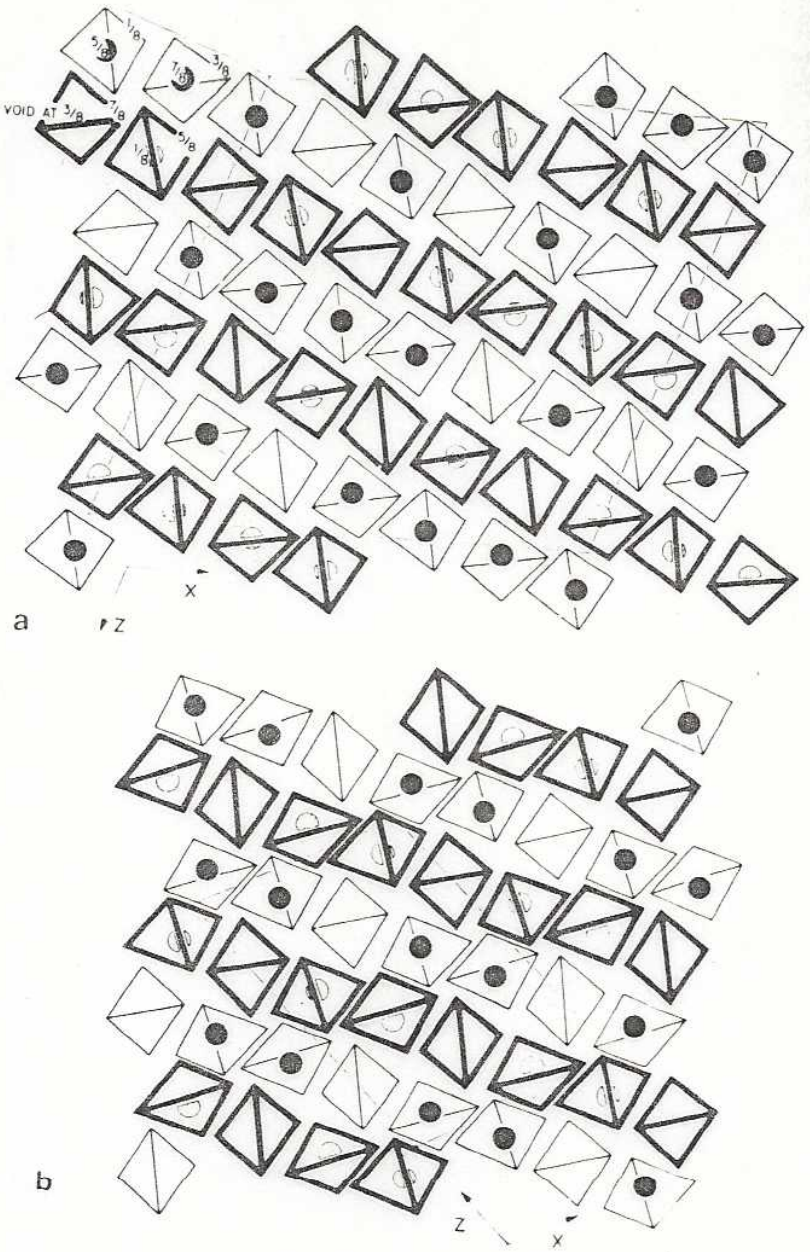

Fig. 30.10. Crystal structures of (a) $La_2(MoO_4)_3$ and (b) $Eu_2(WO_4)_3$. Projections are along the *c* axis of the scheelite subcell, which is outlined in the upper left-hand corner of the $La_2(MoO_4)_3$ structure. Black dots and dotted circles represent La atoms above and below the MoO_4 tetrahedra. The Mo atoms within the tetrahedra are not shown. (From Jeitschko (1973) by courtesy of Acta Crystallogr.)

ferroelectric β'-$Gd_2(MoO_4)_3$ type structure. This latter transition which occurs between 121 (R = Ho) and 235°C (R = Pr) is the basis for the unique properties of these compounds.

The crystal structure of β'-$Gd_2(MoO_4)_3$ was solved independently in two laboratories from twinned (Keve et al., 1971) and single crystals (Jeitschko, 1970, 1972). At high temperature the structure is tetragonal with space group $P\bar{4}2_1m$. Below the transition temperature it is orthorhombic, space group Pba2. The c axis remains practically the same during the phase transition, while the orthorhombic a and b axis are about $\sqrt{2}$ times larger than the tetragonal a axis (fig. 30.11a). The c axis which is nonpolar in the tetragonal form becomes polar in the

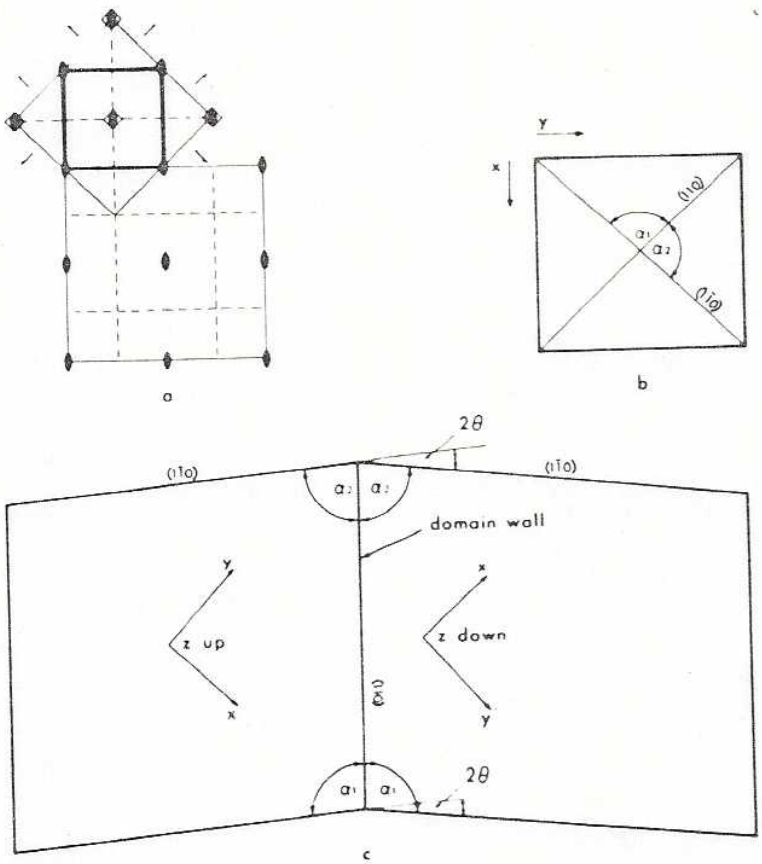

Fig. 30.11. (a) Relation of unit cells of $\beta(P\bar{4}2_1m)$ and β' (Pba2)$Gd_2(MoO_4)_3$. (b) Definition of angles α_1 and α_2. (c) Schematic drawing of a single crystal of ferroic $Gd_2(MoO_4)_3$ with two domains. The {110} planes are cleavage planes and domain walls. The shear angle $\theta = \alpha_1 - \alpha_2$ is the angle between the x direction of one domain and the y direction of the other (From Jeitschko (1972) by courtesy of Acta Crystallogr.)

orthorhombic form. This is the basis for the ferroelectric property: the structure can be switched from one orientation state to the other by an electric field along the c axis. During switching the orthorhombic a and b axes interchange and the c axis inverts. Since the orthorhombic b axis is slightly larger than the a axis, the crystals can be switched also by a compressional stress applied along the b axis. The property was termed *ferroelasticity* by Aizu (1970). The shear angle is a function of the difference between the lengths of the a and b axes (figs. 30.11b, c).

As is usually the case with a displacive phase transition, the crystal structure of the high-temperature (β) form (Jeitschko, 1973) comes close to the average of the (two) different orientation states of the low-temperature (β') form. In both forms the Gd atoms are seven-coordinated and the Mo atoms tetrahedrally coordinated by oxygen atoms. The oxygen atoms have either two or three near metal neighbors (fig. 30.12). The positional differences between the β and β'

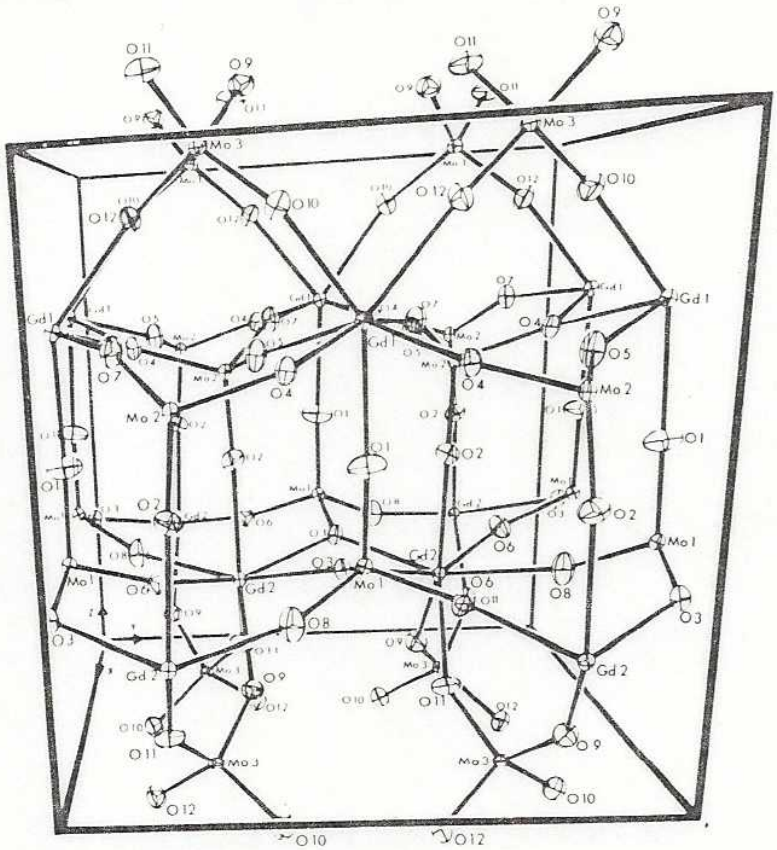

Fig. 30.12. Crystal structure of β'-$Gd_2(MoO_4)_3$. It can be seen that most metal atoms are located in the symmetry-related layers at $z \sim 0.3$ and $z \sim 0.7$ respectively.

form are small (~0.1 Å) for all atoms except for some of the oxygen atoms of certain MoO_4 tetrahedra. Thus the transition from the prototypic (β) to the ferroic (β') phase of $Gd_2(MoO_4)_3$ can be described as the condensation of an oscillatory motion of these MoO_4 tetrahedra. This motion can be seen in the elongated shape of the thermal ellipsoids of some oxygen atoms in the high temperature structure (fig. 30.13).

In the low temperature form the MoO_4 tetrahedra are locked in at either one or the other extreme position in a long-range ordered manner. During ferroelectric (or ferroelastic) switching some MoO_4 groups rotate from one position to the other. The atomic displacements are largest (~0.7 Å) for the oxygen atoms of the switching MoO_4 tetrahedra. The metal atoms move only by about 0.1 Å. The motions occur primarily in the xy plane of the structure. Along the polar z direction the displacements are small and furthermore species (Gd^{3+}, MoO_4^{2-}) with the same charge move mainly against each other in such a way that the change in spontaneous polarisation is small. Thus β'-$Gd_2(MoO_4)_3$ is well described as a canted antiferroelectric.

Since the β to β' phase transition results in a doubling of the primitive cell of the structure, additional (superstructure) reflections occur in the diffraction patterns of the low temperature form. These reflections provide the key to the understanding of the phase transition. Their intensities, angular widths and energies were studied as a function of temperature both above and below the transition temperature (Axe et al., 1971; Jeitschko, 1972; Dorner et al., 1972). The results show that upon heating the temperature-dependent physical properties like spontaneous polarisation, shear angle, and birefringence along the c axis (Cummins, 1970) can be accounted for by gradual shifts in atomic positions toward the high-temperature structure. There is, however, a discontinuity at the transition temperature and in that sense the transition is of first order. The behavior of the structure above the transition temperature is a good example for the soft mode model for displacive phase transitions. Thus, the square of the soft-mode frequency varies linearly with temperature over a wide temperature range. The phase transition, however, occurs about 10°C above the temperature at which the frequency extrapolates to zero. In the temperature range just above the transition temperature the mode is also heavily damped. Thus, the phase transition has also some character of a positional order-disorder transition.

The β'-$Gd_2(MoO_4)_3$ space group, Pba2, is a *allgemeine* subgroup of $P\bar{4}2_1m$, the space group of β-$Gd_2(MoO_4)_3$. Therefore translations as well as other symmetry operations are lost during the β to β' transition. The reduction in point group symmetry ($P\bar{4}2_1m$ to Cmm2) permits the formation of twin domains while the loss of translational operation (Cmm2 to Pba2) allows the occurence of antiphase domains (Jeitschko and Wondratschek, 1974; Wondratschek and Jeitschko, 1976). The ferroelastic–ferroelectric twin domains are of course readily distinguished through their physical (e.g. optical) properties. Antiphase domains are more difficult to observe since they have exactly the same lattice orientation. They are revealed best through the mismatch at their boundary (APB) which results in a higher chemical etching rate at the boundary. The APB's form closed

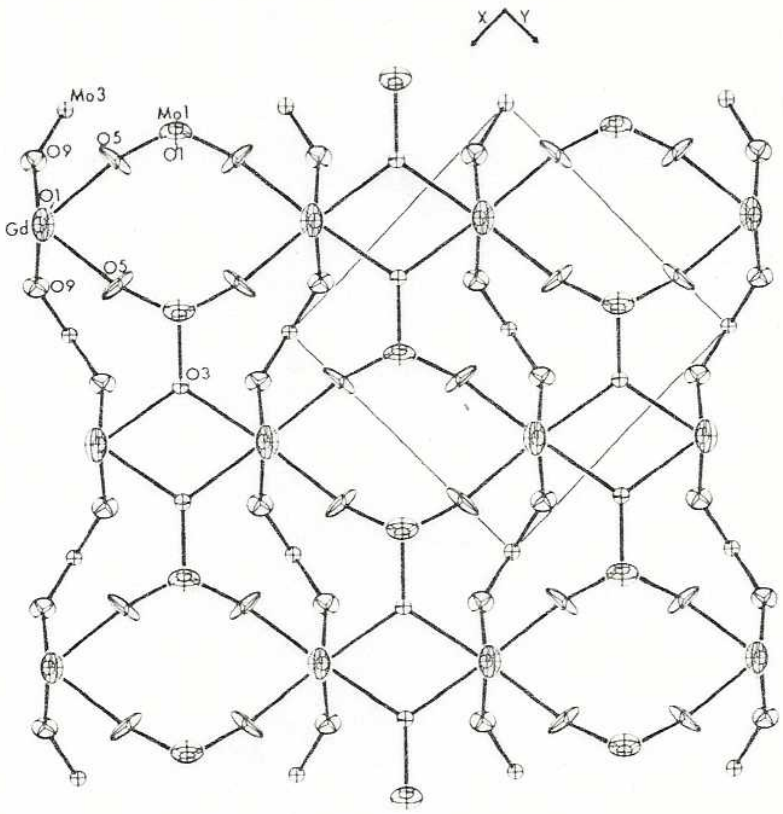

(a)
Fig. 30.13.

loops or terminate on dislocations, external surfaces, or on ferroelectric domain (i.e. twin) walls. They are generated and annihilated by moving domain walls (Barkley and Jeitschko, 1973). On the atomic scale, domain walls correspond to a mismatch in the orientation of MoO_4 tetrahedra in one *or* the other plane perpendicular to the *c* axis, while APB's correspond to a mismatch in *both* planes of the structure (fig. 30.14).

2.1.3. *Molybdates with* $Sc_2(WO_4)_3$ *type structure and amorphous* $R_2(MoO_4)_3$ *compounds*

The $Sc_2(WO_4)_3$ type structure (Abrahams and Bernstein, 1966) occurs for $R_2(MoO_4)_3$ compounds with the small R elements from Ho to Lu. In this structure, which has also been described for $Al_2(WO_4)_3$ by Craig and Stephenson (1968), RO_6 octahedra are linked via all corners to MoO_4 tetrahedra. The MoO_4 tetrahedra share their corners with four RO_6 octahedra. In this way a very open three-dimensional framework is formed.

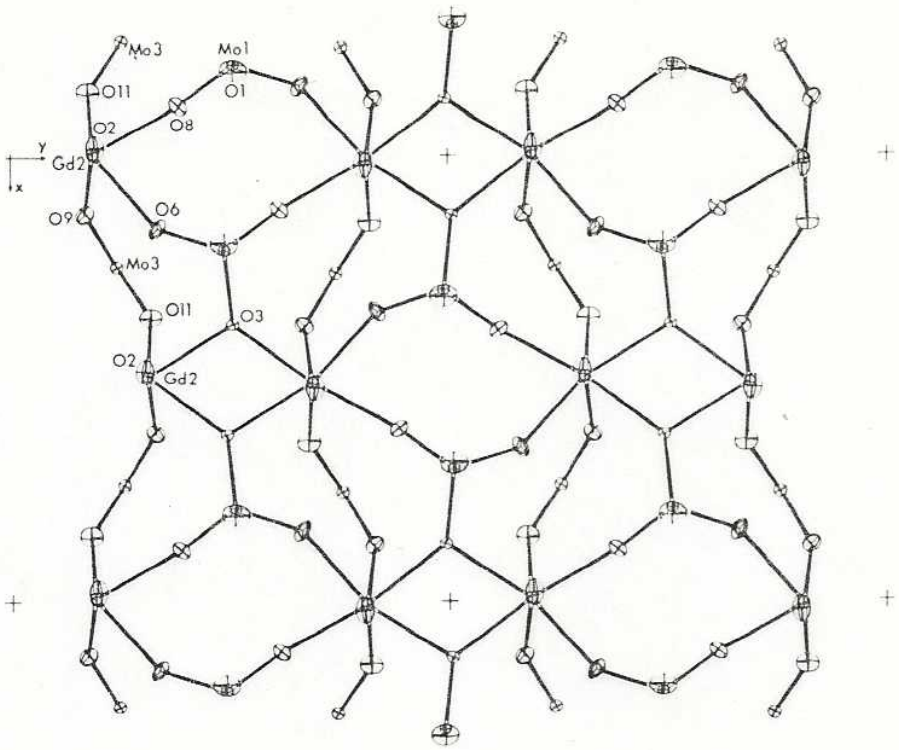

(b)

Fig. 30.13. Comparison of the partial structures at $z \sim 0.3$ of (a) β- and (b) β'-$Gd_2(MoO_4)_3$. Thermal ellipsoids are plotted at the 50% probability limit. (From Jeitschko (1972) by courtesy of Acta Crystallogr.)

In the previously discussed $R_2(MoO_4)_3$ structures the R element is 8-coordinated (defect-scheelites) or 7-coordinated (β-$Gd_2[MoO_4]_3$ type compounds). Correspondingly one third of the oxygen atoms is 3-coordinated in the defect scheelite molybdates, and only one sixth of the oxygen atoms are 3-coordinated (always to two R and one Mo) in β-$Gd_2(MoO_4)_3$. The remaining oxygen atoms are always coordinated to one R and one Mo. Finally in the $Sc_2(Wo_4)_3$ type compounds with 6-coordination for R, all oxygens have coordination number 2. Thus, in going from the large to the small R elements the coordination numbers decrease and the volume per formula unit increases in steps from the defect-scheelites over the β-$Gd_2(MoO_4)_3$ type to the $Sc_2(WO_4)_3$ type compounds. As would be expected, for compositions where two of these basic structure types are found, the lower coordinated structure is always the high temperature form.

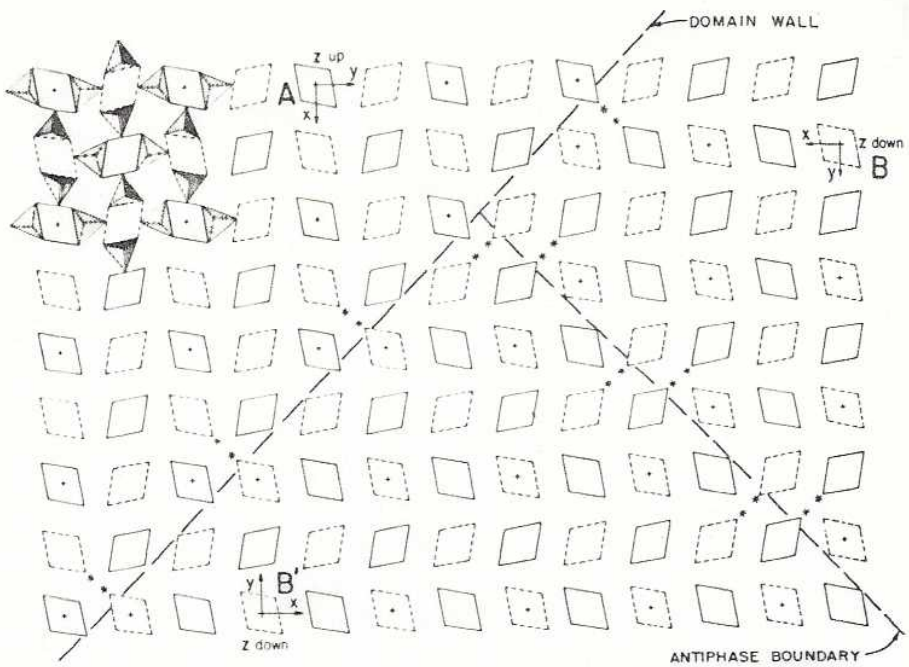

Fig. 30.14. Schematic representation of the β'-$Gd_2(MoO_4)_3$ structure. Diamonds drawn with solid and broken lines represent MoO_4 tetrahedra at two different levels in space. The axis system A, B and B' show the crystal in three different orientation states. States B and B' are parallel (their axis systems are drawn antiparallel in the x and y directions, however, they are parallel through the internal symmetry of the structure) but have a translational mismatch at the antiphase boundary. State A is of opposite polarity. (From Barkley and Jeitschko (1973) by courtesy of J. Appl. Phys.)

Brixner et al. (1971) have shown that the β-$Gd_2(MoO_4)_3$ structure collapses under high pressure to form the higher coordinated $Eu_2(WO_4)_3$ type structure. If the temperature is low (e.g. 25°C) the compound formed is amorphous (Brixner, 1972). A corresponding behaviour can be expected for the molybdates with $Sc_2(WO_4)_3$ type structure. In this way the β-$Gd_2(MoO_4)_3$ type structure could be obtained for the small R elements. Application of high pressure at moderate temperatures should again yield amorphous products.

2.2. *Crystal structures of other* R *molybdates*

Although many more R molybdates with different compositions are described in the literature, few are structurally well characterized. Of the compositions R_2MoO_6 the compounds with R from La to Sm crystallize with the La_2MoO_6 type structure. This structure was determined a long time ago by Sillén and Lundborg (1943) and oxygen positions were only assigned from crystal chemical considerations. It is best described as a layer structure with alternating sheets of

RO_6 octahedra and MoO_4 tetrahedra. The MoO_4 tetrahedra share their corners with RO_6 octahedra of the adjacent sheets above and below. These oxygen atoms are therefore coordinated by one R and one Mo atom. The remaining oxygens belong to the RO_6 layers and are coordinated by four R atoms. The structure of the remaining R_2MoO_6 compounds is probably similar to the structures of Bi_2MoO_6 (Zemann, 1956; van den Elzen and Rieck, 1973) and Bi_2WO_6 (Wolfe et al., 1969) with distorted octahedral oxygen coordination for both R and Mo. In this structure the MoO_6 octahedra share four corners, thus again forming sheets of composition MoO_4 which are interleaved by sheets of composition R_2O_2. For Sm_2MoO_6 which crystallizes with both structural types, the high temperature structure (La_2MoO_6 type) is again the structure with the lower coordination numbers, as was discussed above for compositions $R_2(MoO_4)_3$.

$EuMoO_4$ is reported to crystallize with a scheelite type structure (McCarthy, 1971; Banks and Nemiroff, 1974) and magnetic measurements show that at least most, if not all Mo is in the hexa-valent state (Hubert, 1975). Compounds where Mo has an oxidation number of less than 6 and the large number of mixed molybdates like $CsR(MoO_4)_2$ (Klevtsova et al., 1972) or $K_5R(MoO_4)_4$ (Klevtsov et al., 1975) are outside the scope of the present article.

3. Physical properties (J.R. Barkley)

3.1. *General*

The most interesting physical properties of the described compounds are found in the β-$R_2(MoO_4)_3$ compositions which exhibit the $\bar{4}2m$ to mm2, i.e. β to β', phase transition.

When cooled through the Curie temperature, T_c, the equivalent [110] and [1$\bar{1}$0] axes of the tetragonal phase become the a and b axes of the orthorhombic phase (fig. 30.11). Since these two orthorhombic axes are unequal, the crystal changes shape by a small but significant amount as illustrated in fig. 30.15a and 30.15b. Usually a crystal in the β' phase exhibits several domains which interface along domain walls as shown in fig. 30.15c and 30.15d.

These domains are crystallographically related to each other by the $\bar{4}$ symmetry operation of the β-phase that was lost in the transition. The c-axis reversal across a domain wall is important because the β' phase is polar along c. Thus, the polarization P_s is reversed in adjacent domains.

When an electric field is applied to reverse P_s, the crystal responds by nucleating domain walls along edges. These walls then move sideways to reverse P_s. The hysteresis loop shown in fig. 30.16 relating polarization and applied electric field is characteristic of all ferroelectrics and of the β' phase of $R_2(MoO_4)_3$ as recognized by Borchardt and Bierstedt (1967).

The β-$R_2(MoO_4)_3$ compositions are unusual ferroelectrics however, in that the temperature dependence of the dielectric permittivity ϵ is not Curie–Weiss type

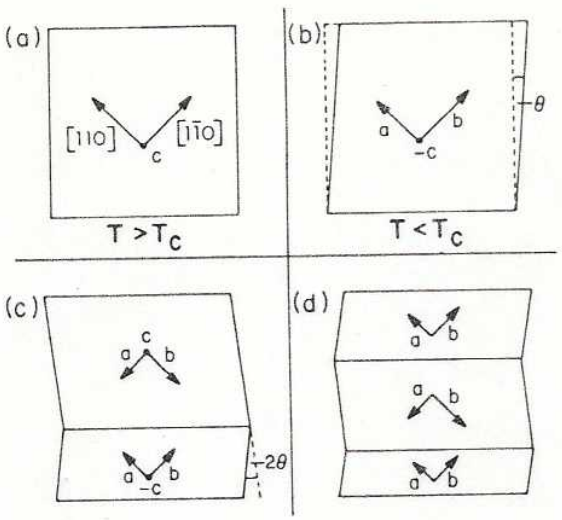

Fig. 30.15. Change in crystal shape observed upon cooling through the $\bar{4}2m$ to mm2 transition in β-$R_2(MoO_4)_3$. For β'-$Gd_2(MoO_4)_3$ at room temperature, the shear angle $\theta = 10'20''$ and $T_c = 159°C$.

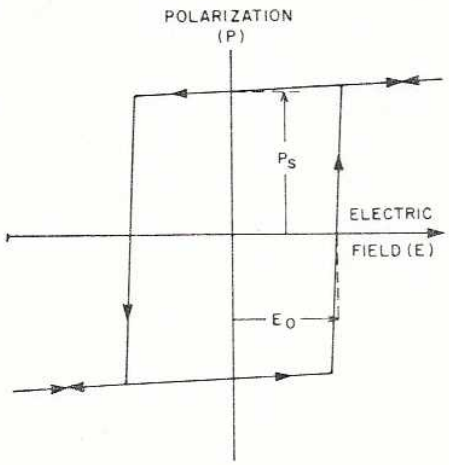

Fig. 30.16. The ferroelectric hysteresis loop relating applied electric field and polarization, both along [001] for β'-$R_2(MoO_4)_3$.

above the Curie temperature. Instead it is certain elastic constants that exhibit large changes when approaching the transition temperature. Cross et al. (1968) observed very little temperature dependence in the small, clamped electric permittivity ϵ_3 of β-$Gd_2(MoO_4)_3$ and a strong temperature dependence in the elastic constant C_{66}^E with an anomaly at T_c. They were led to the conclusion that the spontaneous polarization was an incidental but necessary consequence of the

piezoelectric coupling to the shear strain of the β'-phase relative to the β-phase.

Since then, Pytte (1970), Levanynk and Sinnikov (1970) and Aizu (1971) suggested independently that the β–β' structural change is fundamentally connected with a doubly degenerate soft mode at the Brillouin-zone edge in the β-phase which leads to the doubling of the unit cell.

Direct confirmation of this model was provided by the inelastic neutron-diffraction experiments on β-$Tb_2(MoO_4)_3$ of Dorner et al. (1972). They observed for $T > 159$°C, the frequency ω_M of a doubly degenerate mode at $M(\frac{1}{2}, \frac{1}{2}, 0)$ follows a Curie–Weiss law $\omega_M^2 = A(T-T_c)$ with $A = 0.0165\ \text{meV}^2/°\text{C}$ and $T_c = 149$°C. Their examination of this soft mode showed that the primary order parameter, which necessarily shows large fluctuations near T_c, has no macroscopic polarization, but is instead antipolar. The "freezing in" of this antiferroelectric static displacement however, couples to the shear strain χ_{12} which in turn produces the polarization by piezoelectric coupling. They show that observed temperature dependences of P_s and χ_s are proportional to the square of this order parameter. Other studies have also supported or at least have been consistent with this description of the transition; for example, Raman scattering by Fleury (1970) and Ganguly et al. (1975); infrared absorption data of Petzelt et al. (1971) and Dvorak (1971); the temperature dependence of the elastic constants by Epstein et al. (1970), Hochli (1972), Courdille et al. (1973, 1975), Chizhikov et al. (1971), and the lattice dynamics calculations of Boyer and Hardy (1972, 1973).

The importance of the "elastic" properties of the β-$R_2(MoO_4)_3$ compositions has stimulated definition of a phenomenon called "ferroelasticity" a term coined by Aizu (1969).

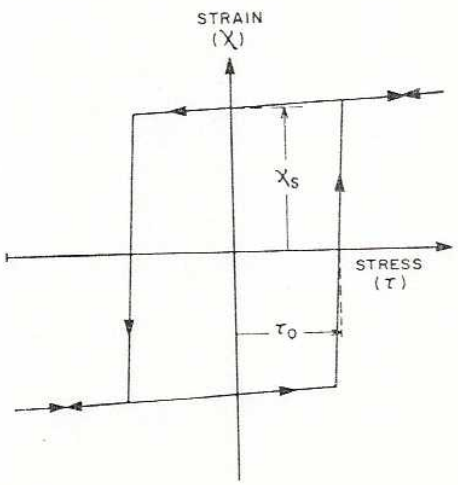

Fig. 30.17. The ferroelastic hysteresis loop relating applied stress and strain, both in the (001) plane, for β'-$R_2(MoO_4)_3$.

A material is said to be ferroelastic if it has two or more stable orientational states in the absence of mechanical stress and if it can be reproducibly transformed from one to another of these states by the application of mechanical stress. (Further discussions of ferroelastic behavior can be found in Aizu (1971b, 1974), Abrahams et al. (1971a,b), Sapriel (1974), Toledano (1974), Janovec (1976).) A ferro-elastic "hysteresis loop" analogous to the ferroelectric loop is also observed in β-$R_2(MoO_4)_3$ as shown in fig. 30.17 (see Kumada, 1969, 1970). The β'-phase of $R_2(MoO_4)_3$ is called a coupled ferroelectric/ferroelastic which means that polarization reversal necessarily accompanies the strain reversal and vice-versa. Ferroelasticity, like ferroelectricity, is a structure dependent property and is directly inferrable from the point group symmetry change $\bar{4}2m$ to mm2 at the transition as described in Aizu's (1969) paper.

The hystersis loops of fig. 30.16 and 30.17 improperly imply that the switching process for strain or polarization reversal is instantaneous and complete once the threshold field, E_0 or stress τ_0 is exceeded. This switching occurs by domain wall nucleation and movement which is not particularily fast for the β'-molybdates. Much of the "applied" research on these materials concerns this switching process as summarized in ch. 30 section 3.6.

3.2. *Electrical properties*

As already discussed, the polarization-field relationship is given by the hystersis loop of fig. 30.16. The temperature dependence of P_s for $Gd_2(MoO_4)_3$ as

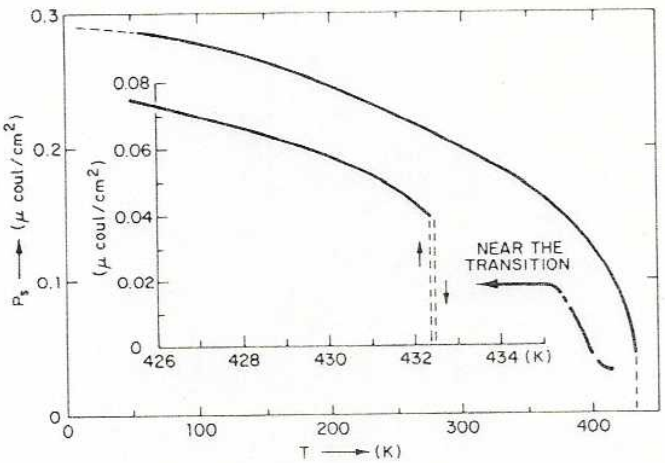

Fig. 30.18. Spontaneous polarization as a function of temperature in β-$Gd_2(MoO_4)_3$ single crystal. Above 75 K, P_s is deduced from low-frequency (0.01 Hz) isothermal loops. Below 75 K, P_s is measured from pyroelectric charge and discharge of single-domain samples (Sawaguchi and Cross, 1973).

measured by Sawaguchi and Cross (1973) is shown in fig. 30.18, and agrees with similar data of Aizu et al. (1969) and Cummins (1970). The first order nature of the transition is evident in the marked jump in P_s at the transition. Both Sawaguchi et al. (1973) and Kumada (1974) observed that the β to β' transition could be forced by applying an electric field to a crystal held slightly above T_c, i.e., in the β phase. In this case double hysteresis loops are observed, further evidence of the first order nature of the transition.

Room temperature values for P_s for selected β'-$R_2(MoO_4)_3$ compositions are given in table 30.7. The measured value for $Gd_2(MoO_4)_3$ agrees reasonably well with values estimated by Keve et al. (1971) and Jeitschko (1972), whereby P_s is due almost entirely to the MoO_4 group rearrangement and the Gd^{3+} ions play no essential role.

The pyroelectric properties of $Gd_2(MoO_4)_3$ were measured by Ullman et al. (1972 and 1975). They found that $Gd_2(MoO_4)_3$ single crystals operated close to T_c have figures of merit for pyroelectric responsivity comparable to presently utilized pyroelectric detector materials, e.g. Triglycine Sulfate. However, when operating near T_c, they encountered hard-to-control spurious domain nucleation due to small thermal gradients caused by the thermal signal being detected, even though a large biasing field was used to attempt to maintain a single domain state. (Also see Nakamura et al. (1971b) and Kumada (1973) for other field effects near T_c and Shirokov (1972) and Midorikawa et al. (1974) for hydrostatic pressure effects on T_c.)

Both β and β' phases of $R_2(MoO_4)_3$ are piezoelectric. The temperature dependence of the piezoelectric constants d_{31} and d_{33} as measured by Scheiding et al. (1973) is given in fig. 30.19. At room temperature, $d_{31} \doteq -1.5 \times 10^{-12}$ m/V and $d_{33} \doteq 0.5 \times 10^{-12}$ m/V.

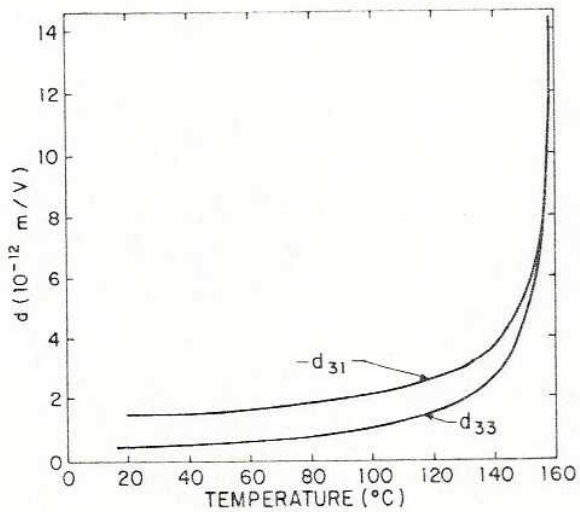

Fig. 30.19. Temperature dependence of the piezoelectric coupling constants d_{31} and d_{33} for β'-$Gd_2(MoO_4)_3$ (Scheiding et al., 1973).

TABLE 30.7.
Room temperature properties of selected β'-$R_2(MoO_4)_3$ compositions.

Composition	Lattice constants (l)			T_c (β–β')	χ_{ab}[a]	P_s	Wall mobility		Optical[b]	
	a(Å)	b(Å)	c(Å)	(°C)	(10^{-3})	(10^{-2} C/m^2)	μ_E (10^{-6} m^2/V s)	μ_τ (10^{-6} m^3/N s)	n_a	Δn_{ab} (10^{-4})
$Pr_2(MoO_4)_3$	10.5255	10.5782	10.9013	235.0 [1]	2.497	–	–	–	2.20 [5]	1.9
$Nd_2(MoO_4)_3$	10.4966	10.5426	10.8544	244.9 [1]	2.186	–	–	–	1.75 [5]	2.7
$Sm_2(MoO_4)_3$	10.4352	10.4718	10.7687	197.2 [1]	1.751	>0.24 [3]	–	–	–	–
$Eu_2(MoO_4)_3$	10.4109	10.4436	10.7269	180.5 [1]	1.568	0.14 [3]	–	–	–	–
$Gd_2(MoO_4)_3$	10.3881	10.4194	10.7007	159.5 [1]	1.504	0.21 [3]	2.1 [6]	3.2	1.85 [7]	4.08
$GdTb(MoO_4)_3$	10.3688	10.3982	10.6766	~162 [8]	1.416	–	2.1 [6]	3.1	–	–
$GdDy(MoO_4)_3$	10.3582	10.3837	10.6564	155. [2]	1.229	0.19 [5]	1.2 [6]	1.8	1.84 [5]	4.1
$Tb_2(MoO_4)_3$	10.3518	10.3807	10.6531	160. [2]	1.394	0.18 [3]	2.2 [6]	2.9	1.89 [5]	3.7
$Dy_2(MoO_4)_3$	10.3271	10.3513	10.6145	145. [2]	1.170	–	–	–	–	–
$Gd_{1.3}Ho_{0.7}(MoO_3)_4$	10.3593	10.3831	10.6606	153.3 [8]	1.147	–	0.66 [5]	–	–	–
$Ho_2(MoO_4)_3$	10.3038	10.3244	10.5783	121.0 [1]	0.999	–	–	–	–	–

[a] $\chi_{ab} \equiv (b-a)/(b+a)$ (l). [b] Refractive indices given for $\lambda = 6328$ Å.

References [1] Brixner et al. (1972); [2] Brixner et al. (1971); [3] Borchardt et al. (1967); [4] Sawaguchi et al. (1973); [5] Barkley, unpublished; [6] Flippen (1975); [7] Kumada (1972); [8] Brixner, unpublished.

These values are somewhat lower than Kumada's (1969) earlier measurements. The electromechanical coupling coefficient k_3 was measured by Cummins (1970) to be about 4% at room temperature increasing to about 22% near T_c.

The presence of domain walls significantly influences the resonant behavior of a crystal. Often a particular crystal shape will promote a multidomain state. This frustrates excitation of whole crystal resonances because the sign or sense of the piezoelectric distortion is reversed in opposing domains. A domain wall moving into a previously single domain crystal has the same effect as reversing the [001] field direction in the crystal behind the wall. Thus, the region behind the wall is distorting out of phase relative to the rest of the crystal and unless the wall(s) is (are) judiciously placed relative to nodes, (see Newnham et al. (1975)) crystal resonances are frustrated.

3.3. *Elastic*

The thermal expansion of $Gd_2(MoO_4)_3$ has been measured by Newnham et al. (1969) and Cummings (1970) by X-ray powder and dilatometric methods respectively. However, by X-ray study of a $Gd_2(MoO_4)_3$ single crystal by Kobayashi et al. (1973) is most recent and thorough. Their data on the temperature dependence of the lattice constants and lattice volume are given in fig. 30.20. The first order nature of the transition is seen as a small discontinuous change in lattice constant with a thermal hysteresis of about 3.5°C as seen in fig. 30.21.

The spontaneous lattice strains χ_1, χ_2, and χ_3 along the a-, b-, and c-axes and the pure shear χ_{12} in the (001) plane are presented in fig. 30.22 (Kobayashi et al., 1972).

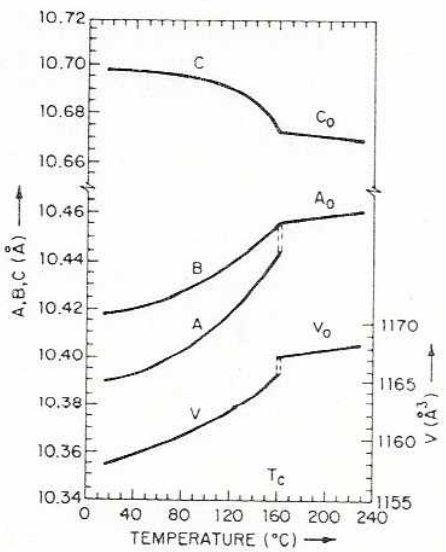

Fig. 30.20. Temperature dependence of the a-, β-, and c-lattice parameters, and the lattice volume V of β-$Gd_2(MoO_4)_3$ (Kobayashi et al., 1972).

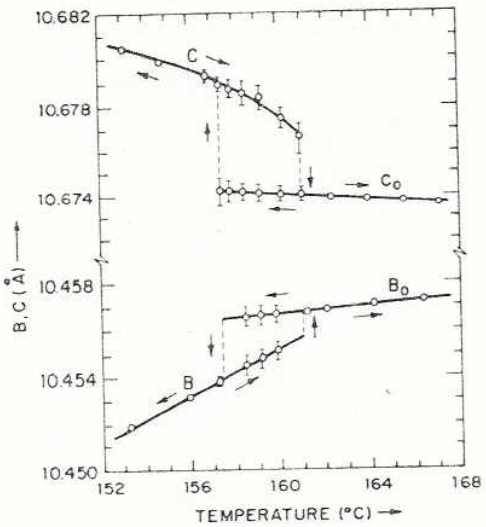

Fig. 30.21. Temperature dependence of the b- and c-parameters of $Gd_2(MoO_4)_3$ in the neighbourhood of the Curie temperature (Kobayashi et al., 1972).

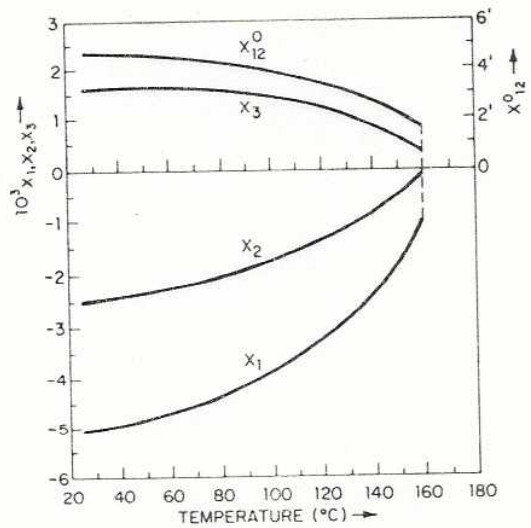

Fig. 30.22. Spontaneous lattice strains χ_1, χ_2, and χ_3 along the a-, b-, and c-axes of β'-$Gd_2(MoO_4)_3$ as a function of temperature. The pure shear χ_{12} in a plane perpendicular to the c-axis is also indicated (Kobayashi et al., 1972).

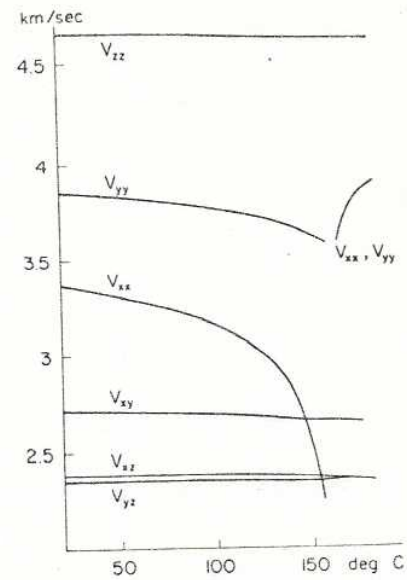

Fig. 30.23. Sound velocities in β-$Gd_2(MoO_4)_3$. Curves are labeled by propagation axis and polarization axis. xy denotes the axis bisecting x and y. Data taken at zero electric field (Höchli, 1972).

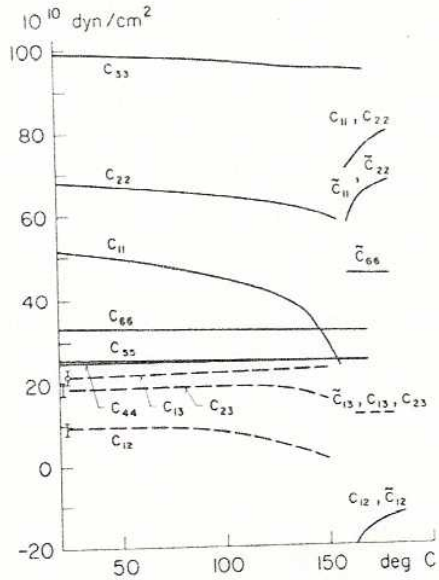

Fig. 30.24. Temperature dependence of the elastic constants in $Gd_2(MoO_4)_3$. The $\tilde{C}$ notation refers to the tetragonal axes that are rotated 45° around [001] relative to the orthorhombic (β') axes (Höchli, 1972).

The spontaneous strain $(\chi_{12})_s$ may be reversed, as discussed earlier, with fig. 30.17, by applying a compressional stress along the orthorhombic b-axis. At very small applied stress, the crystal responds with a small elastic deformation until the critical threshold stress (τ_0) is exceeded at which time domain walls nucleate and move until the region subjected to the stress has been "switched" to the opposite strain state. Decreasing this applied stress to zero leaves the crystal in the "positive", χ_s spontaneous strain state.

Domain wall behavior during this switching process has attracted interest because most device applications in some way involve domain wall movement to modulate electromagnetic or acoustic energy. Domain wall dynamics will be discussed in section 3.6.

Hochli (1972) measured the temperature dependence of sound velocities in $Gd_2(MoO_4)_3$ as shown in fig. 30.23 and the elastic constants given in fig. 30.24 and table 30.8. The softening of the lattice at the β-β' transition is obvious from these data.

TABLE 30.8.
Elastic constants in gadolinium molybdate[a].

Temp. (°C)	C_{11}	C_{22}	C_{33}	C_{44}	C_{55}	C_{66}
22	51.6	67.6	98.2	25.1	25.8	33.4
60	49.7	66.2	97.8	25.0	25.7	33.1
100	46.9	64.9	97.2	24.9	25.6	32.5
140	41.5	62.4	96.7	24.7	25.5	31.9
159	32.9	59.5	96.2	24.7	24.8	31.6
160	70.5	70.5	96.0	24.7	24.7	31.6
180	77.0	77.0	95.0	24.7	24.7	31.6

[a]Table kindly provided by Höchli in private communication (1972).

3.4. *Optical*

β-$R_2(MoO_4)_3$ boules can be grown that have excellent optical quality. However growth conditions which promote precipitation of other phases such as α-$R_2(MoO_4)_3$ or R_2MoO_6 must be carefully avoided as described in section 3.1. When present, these second phases introduce optical scattering that is easily observed under laser illumination. Optical scattering is also caused by degradation of (001) surfaces in a moist atmosphere or from fingerprints. Under these conditions, small, shallow etch pits slowly develop where dislocations exit these surfaces. This problem is eliminated when (001) surfaces are coated with chemically stable thin films of indium or tin oxide which are often used as transparent electrodes.

$Gd_2(MoO_4)_3$ is transparent between ~2000 and 28 000 cm^{-1}. Other β-$R_2(MoO_4)_3$ materials exhibit colors typical of rare earth ions in a highly asymmetric site. UV

excited fluorescence was observed by Borchardt et al. (1965, 1966) and Bagdasarov et al. (1971). Borchardt saw laser action at room temperature in $Gd_2(MoO_4)_3$ + (~3 wt% Nd^{3+}) crystals in the wavelength range 1.045 to 1.09 μm.

The Raman spectra of the β-$R_2(MoO_4)_3$ compositions is discussed by Scott (1974) and Shepherd (1972) in addition to those references given in section 3.1.

β'-$R_2(MoO_4)_3$ single crystals are optically positive and biaxial (Smith and Burns, 1969). The optic axes are in the (100) plane with the acute bisetrix along [001]. The wavelength dependence of the refractive index is given in fig. 30.25 for several $R_2(MoO_4)_3$ compositions.

The temperature dependence of Δn_{ab} measured by Smith and Burns (1969) and Cummins (1970) follows approximately the temperature dependence of P_s and χ_s shown in fig. 30.18 and 30.22. But Nakamura et al. (1971) and Kumada (1972) pointed out that in an applied field or stress both the polarization and strain of a single domain crystal are observed to increase, but the birefringence decreases as shown in fig. 30.26. The observed field dependence of the birefringence in the β' phase has the same sign and approximately the same magnitude as that observed in the β-phase. The spontaneous birefringence is thus not caused by the internal field produced by P_s, but rather is directly caused by the ion displacements within a unit cell (as described by the order parameter discussed in section 3.1) which only incidently causes the macroscopic strain and polarization.* Further discussion and measurements of electrooptic properties of β-

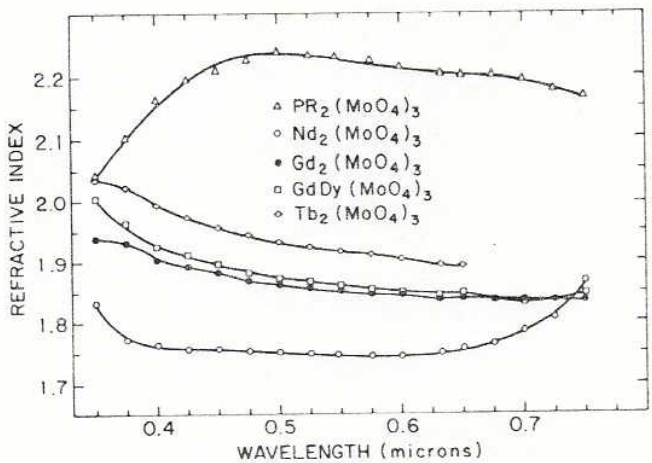

Fig. 30.25. Index of refraction versus wavelength for several β'-$R_2(MoO_4)_3$ single crystal compositions.

*W. Jeitschko and W. Bindloss (private communication) have pointed out that the ion positions *within* a unit cell in β'-$R_2(MoO_4)_3$ would provide the orthorhombic symmetry (and presumably the birefringence) even if the a- and b-lattice constants were equal. The large rotation of certain molybdate groups cooling through T_c forces a and b to become unequal which, of course, is the macroscopic strain χ_s. This χ_s in turn causes P_s through piezoelectric coupling.

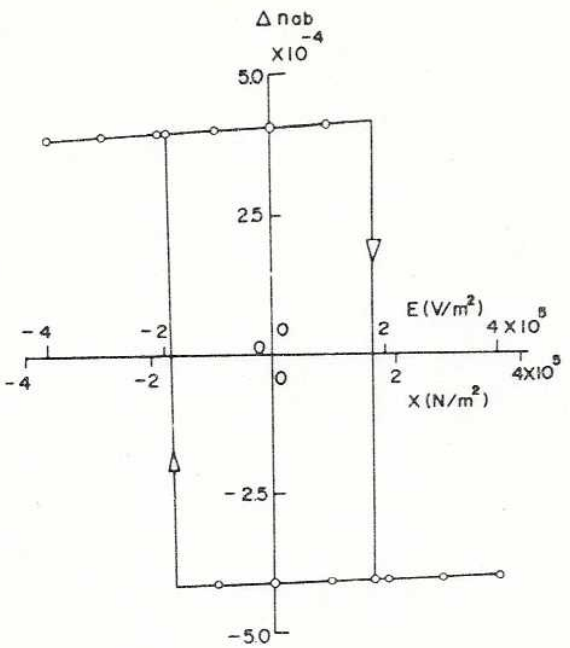

Fig. 30.26. Birefringence Δn_{ab} versus applied field and stress for β'-$Gd_2(MoO_4)_3$ at room temperature (Kumada, 1972).

$R_2(MoO_4)_3$ can be found in Miller et al. (1970) and Fousek and Konak (1972).

The scattering of light by acoustic waves in single and multidomain crystals of β'-$Gd_2(MoO_4)_3$ has been studied by Esayan et al. (1974). They determined all 12 independent photoelastic constants and found the constant p_{66} of opposite sign relative to p_{11}, p_{22}, p_{12} and p_{21}. Thus both electrooptic and elastooptic constants associated with the shear deformation about [001] appear to be negative.

The domain structure in β'-$R_2(MoO_4)_3$ single crystals is readily visible when viewed along [001] between crossed polarizers. Mutually orthogonal conoscopic figures are observed in opposed domains, see Kumada (1972). This means that the optic plane rotates about [001] by 90° as a domain wall moves across the crystal. Therefore, a (001) polished plate prepared with a thickness that provides a quarter wave retardation in one domain (about 0.033 cm for $Gd_2(MoO_4)_3$ at $\lambda = 5500$ Å) will have a negative quarter wave retardation in the opposing domain. Incident light directed along [001] and linearly polarized along (110) will exit one domain with right circular polarization and the opposing domain with left circular polarization. A crystal observed through a circular polarizer, alternately blocks or transmits the light upon repeated switching. This property of highly transparent β'-$Gd_2(MoO_4)_3$ has stimulated proposals for novel device applications throughout the world. For further discussion of several device applications for β'-$R_2(MoO_4)_3$ materials see Smith and Burns (1969), Kumada (1969, 1972) and Barkley et al. (1972).

3.5. *Magnetic*

Both β-$Gd_2(MoO_4)_3$ and β-$Tb_2(MoO_4)_3$ are paramagnetic at room temperature with moments 7.98 μ_B and 9.65 μ_B respectively (Keve et al., 1970). They also found that both compositions remain paramagnetic down to 1.4 K. Fisher et al. (1975) have found that these compositions become antiferromagnetic below 0.3 K and ~2 K respectively.

An extensive investigation of the low temperature magnetothermodynamics of β'-$Gd_2(MoO_4)_3$ and β'-$Tb_2(MoO_4)_3$ is presented in a series of papers; (Fisher et al., 1972; Hornung et al., 1972; Brodale et al., 1972; Fisher et al., 1973; and Fisher et al., 1975).

3.6. *Domain walls*

Many domain walls can exist simultaneously in a crystal, as shown in the photograph of fig. 30.27 taken with transmitted light in a polarizing microscope. Although various wall configurations are shown in the figure, walls develop primarily along two orthogonal crystallographic planes (110) and ($\bar{1}$10).

The simplest type of wall is planar and extends across the whole crystal, as sketched in fig. 30.15c and 30.15d. When two orthogonal plane walls are driven into each other with an applied field or stress, the strain that develops at their intersection fractures the crystal. These intersections are avoided when only parallel walls switch a crystal.

Some mention of the importance of the crystal shape seems desirable. The shape of a crystal influences the overall strain pattern and thus the wall configurations that form easiest in that crystal. Domain walls tend to nucleate easily along crystal edges that are not (110) surfaces. Fig. 30.28a shows a crystal shape which promotes formation of two sets of orthogonal walls which readily move in away from the edges. A circular (001) plate may do likewise and attempts to switch it with field or stress will eventually force two perpendicular walls against each other to fracture the crystal.

A crystal shape improved to sustain a greater number of switching cycles has at least 2-edges parallel to (110) planes as shown in fig. 30.28b.

A further refinement to provide a crystal of a potentially long lifetime is to trap a single wall as shown in fig. 30.29. A crystal of this configuration with indium oxide electrodes, has sustained $>10^9$ switching cycles successfully (Barkley et al., 1972).

Crystals mounted in this way can be used to investigate the field and stress dependence of the planar wall velocity.

Kumada et al. (1970) observed that the "sideways" velocity of domain walls driven by electric field increased linearly with fields applied along [001]. Walls may also be driven with shear stress in the (001) plane. Reversing either stress or field direction reverses the direction of wall movement. Flippen (1975) has found that stress and electric field effects on wall velocity are additive following the expression

$$v = \mu_\tau(\tau - \tau') + \mu_E(E - E'); \qquad \tau > \tau_0 \text{ and } E > E_0,$$

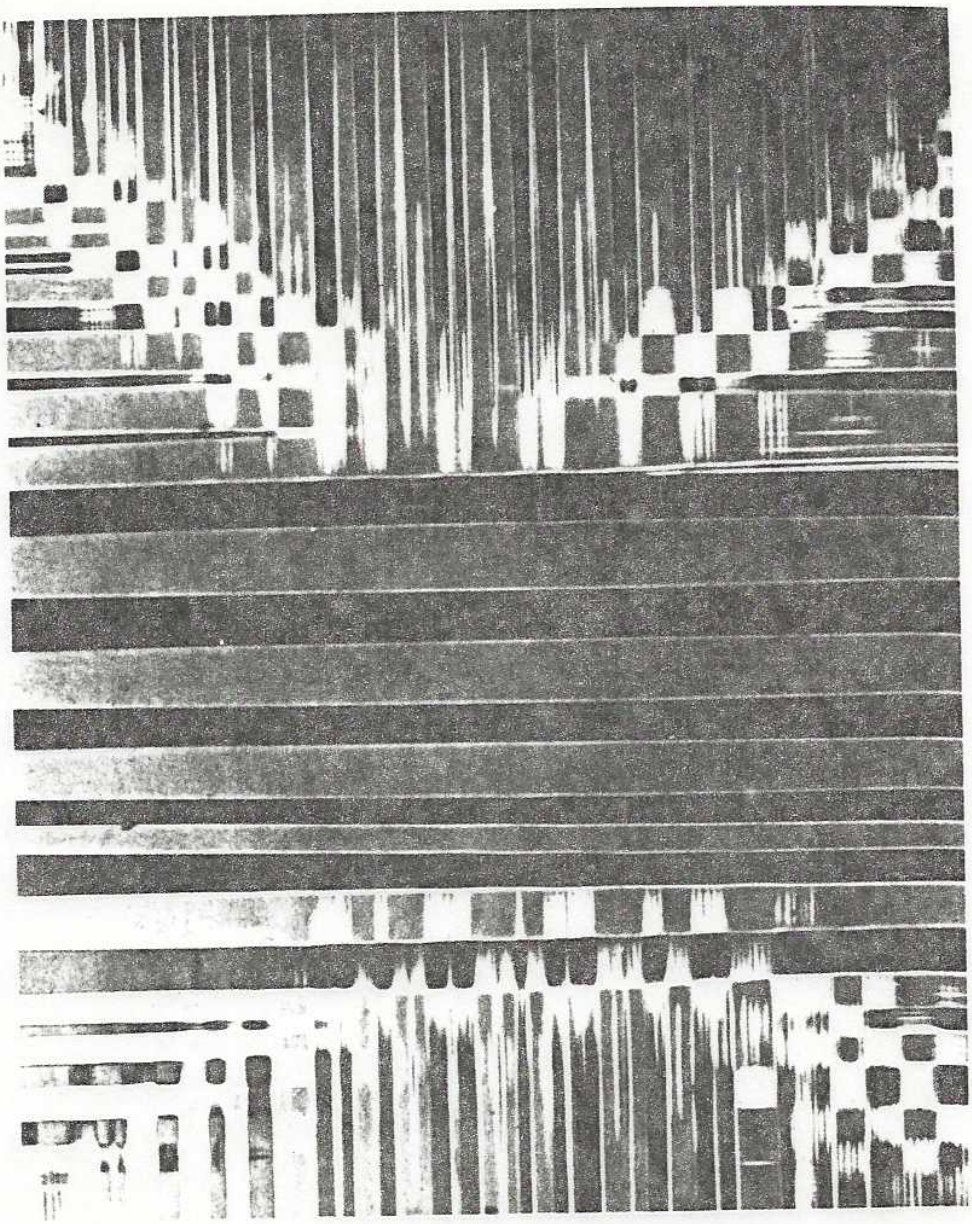

Fig. 30.27. Domain walls observed in a circular (001) plate of β'-$Gd_2(MoO_4)_3$ after cooling through T_C.

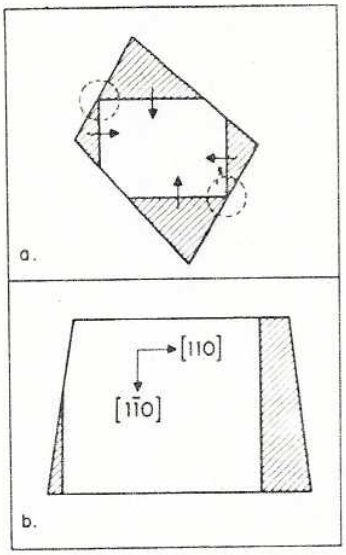

Fig. 30.28. The shape of (001) plates can promote destructive wall intersections (circled in (a)) during switching with field or stress. A crystal shaped to avoid wall intersections as in (b), will promote switching with only parallel walls.

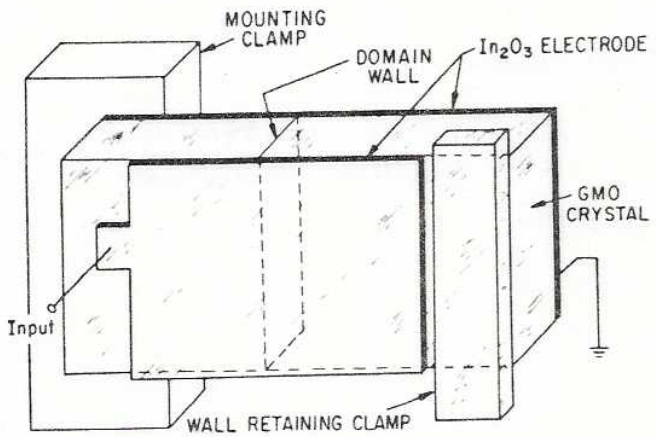

Fig. 30.29. Design for mounting and electroding GMO crystals to suppress nucleation and growth of unwanted domains. A single domain wall permanently retained in the crystal is used to switch the region between the clamps (Barkley et al., 1972).

where the mobilities μ_τ and μ_E are given in table 30.6 for various $R_2(MoO_4)_3$ compositions τ' and E' are "offset" values that appear to be more sensitive to composition and "character" of the electrode-crystal interface than to internal crystal defects (Barkley, unpublished). The threshold stress τ_0 and field E_0 are those required to initiate wall movement and are sample dependent varying with defect density, second phase concentration, electroding conditions, residual strain, etc.; see Barkely et al. (1972) and Kumada (1973). Under the best conditions and best samples, E_0 values as low as 100–200 volts/cm have been observed. The wall mobilities are fairly insensitive to most of these factors, and depend primarily on the sample composition. The wall mobilities are also temperature independent (Kumada, 1970) up to about 80°C at which temperature the mobility increases and crystals tend to form many domains rather than move a single wall in response to the applied field.

Flippen (1975) also observed that the electric field just sufficient to balance an oppositely directed mechanical stress was independent of the compositions tested, i.e., $Gd_2(MoO_4)_3$, $Tb_2(MoO_4)_3$, $GdDy(MoO_4)_3$ and $GdTb(MoO_4)_3$. These compositions have different field and stress mobilities, and the fact that these results are composition independent may suggest that the domain wall velocity is determined primarily by structure factors.

Work along this line has been done by Bornarel (1975) in KH_2PO_4 where he describes domain wall movement in terms of a succession of small steps, jogs or twinning dislocations that move rapidly along the surface of a domain wall. The passage of each step translates the wall a small distance, presumably a lattice spacing. Thus at high domain wall velocities, this step velocity may already approach the speed of sound in these materials. Perhaps a phonon-drag mechanism such as described in Frost and Ashby (1971), may be operative in which under certain conditions a linear relationship exists between the velocity of the (twinning) dislocations along the surface of the wall and the driving force on these dislocations. A useful starting point to interpret the observed domain wall behavior may be to consider the energy loss to the lattice during the rapid rotation of the molybdate groups as a twinning dislocation moves during wall movement.

Normally domain walls in the $R_2(MoO_4)_3$ materials tend to remain planar, but certain conditions can occur, deliberately or otherwise, which can bend them. In fact, fig. 30.27 shows slightly bent (110) walls that form very thin blade-like domains, similar to those observed by Bornarel (1975) in KH_2PO_4 and Kursten et al. (1973) in $Gd_2(MoO_4)_3$. Wall configurations involving these "blade" domains can be nucleated and moved controllably with strong field or stress gradients in the crystals (Barkley – unpublished results). The tips of blade domains move parallel their length at field mobilities between $1–3 \times 10^{-4}$ m^2/(V sec), much higher than the mobility for sideways motion of planar walls.

Another interesting wall configuration that appears to be metastable is called a zigzag wall by Flippen and Haas (1973) and is shown in fig. 30.30. This zigzag (zz) wall appears to be made up of ordinary planar walls which have been bent out of their usual (110) planes (which are vertical and normal to the plane of the figure). These bent walls intersect tangentially at the zz tips.

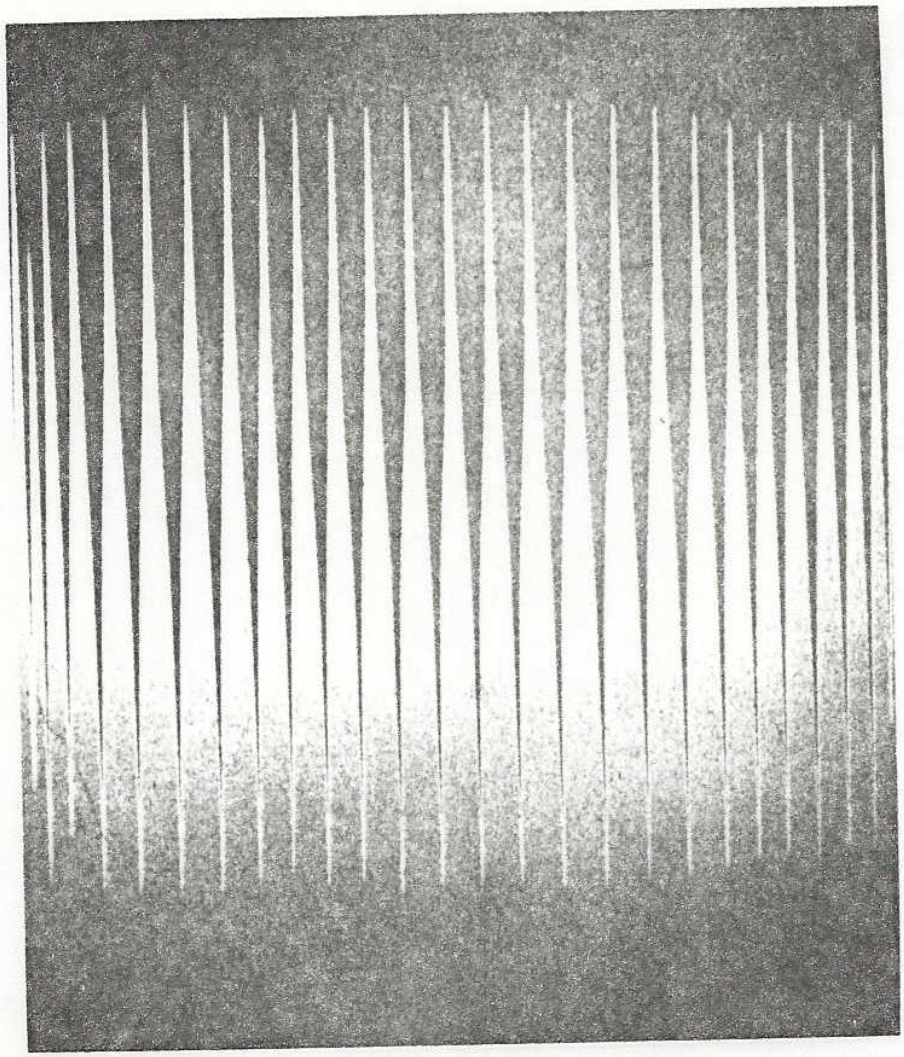

Fig. 30.30. Photograph of a zigzag domain wall in β'-$Gd_2(MoO_4)_3$ viewed between crossed polarizers in transmitted light.

Under field or stress, the zz wall moves sideways, i.e., vertically in fig. 30.30, while retaining essentially the same shape. Individual tips remain in the same (110) planes as the zz wall moves across the crystal. The observed zz wall mobility is 20 to 30 times higher than the planar wall mobility.

Individual tips of this zz can be extended if an electric field is applied immediately over the tip. Such tips have been observed to move at about 10^2 m/sec, i.e., about 10% of the velocity of sound. This is much faster than the observed net velocities of the whole zigzag wall. (This observation suggests that

if twinning dislocation motion is a reasonable description of domain wall movement, then these dislocations must be moving at least 10% the sound velocity in these blade tips.)

The actual width of domain walls in β'-$Gd_2(MoO_4)_3$ has been the subject of several articles. Domain Walls in ferroelastics would tend to be thicker than strain-free domain walls found in ferroelectrics. This thicker wall reduces the strain energy in the wall. Direct observations of a wall in a polarizing microscope suggests a wall thickness of a few microns (Shepherd and Barkley, 1972) but this observation is complicated by refraction and diffraction of the transmitted light in the region of the wall. Observation of the diffraction pattern from a wall in a (001) plate having a halfwave retardation suggested a wall thickness of 1.3 μm (Suzuki, 1973). Shepherd and Barkley (1972) using Raman scattering from the distorted material in a moving wall estimated a wall thickness greater than $\sim$0.8 μm. However, antiphase boundaries which were discovered later (Barkley and Jeitschko, 1973 and Meleshina et al., 1974), could also have contributed to the observed Raman signal. thus the estimate of 0.8 μm from the Raman data could very well be high.

Berg–Barrett X-ray data (Bindloss and Moore, unpublished) suggest a planar wall thickness of less than 1 μm. Kittel (1972) estimated a wall thickness in β'-$Gd_2(MoO_4)_3$ of $\sim$ 0.4 μm from the free energy difference between β and β' phases as derived from the specific heat data of Fouskova (1969).*

A second estimate of the wall thickness was made by Haas and Jaep (1974) by considering the material in the wall as elastically strained β'-phase. Their estimated thickness is $\sim$0.8 μm. However, the energy per unit surface area of the wall in Kittel's model was estimated to be $\sim$100 ergs/cm^2 as compared with Haas and Jaep's 0.1 erg/cm^2. It would seem that future experiments on wall energies will differentiate between these estimates, a factor of 10^3 apart.

Thus, at this time, the evidence seems to indicate a wall thickness $\leq$1 μm, which is indeed much thicker than the pure ferroelectric domain walls which are commonly thought of as a few lattice dimensions thick (Cohen, 1951).

3.7. *Crystal defects*

Crystal defects impede domain wall movement by increasing E_0 and τ_0, the minimum field and stress needed to initiate motion. For this reason, studies of chemically etched surfaces of $Gd_2(MoO_4)_3$ have been done to investigate the nature of these defects. Kashiwada and Kishino (1974) have used chemical etchants and X-ray transmission topography to identify flat helical dislocations and flat closed loop dislocations that have axes parallel [110] directions. Although these authors did not report on the interaction of these defects with

*Later specific heat data by Cheung and Ullman (1974) also agrees with Fouskova's transition entropy estimate $\sim$0.22 cal/mole K. T_c is observed to increase linearily with hydrostatic pressure at the rate $\delta T_c/\delta_p = 29.5 \pm 0.3$ deg/kbar (Shirokov, 1972). Their estimate of the transition entropy $\Delta s = 0.17$ cal/mole deg also agrees reasonably well with Fouskova's.

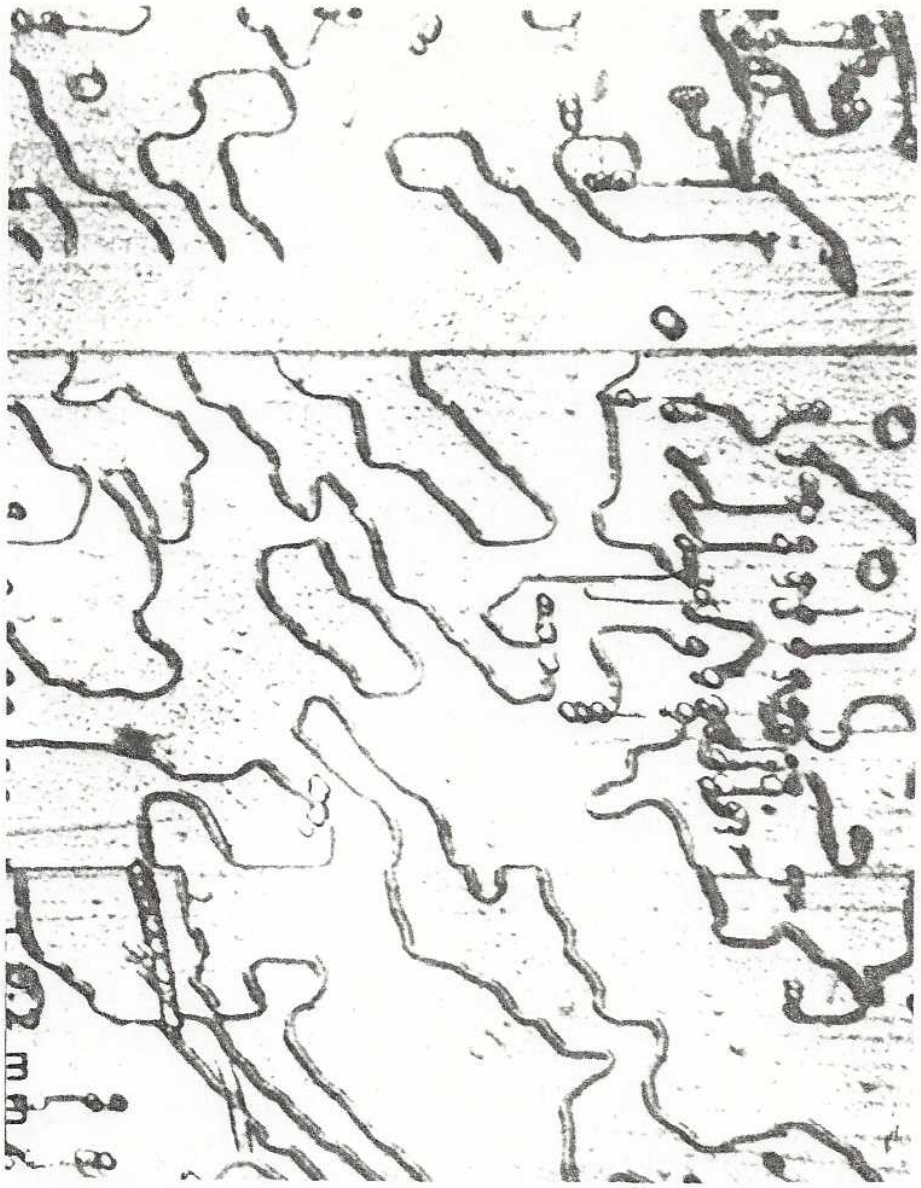

Fig. 30.31. Photomicrograph on an etched (001) surface of $Gd_2(MoO_4)_3$ taken in reflected light. Trench-like etch pits develop along APB's in the negatively charged surfaces but not in the positively charged surface in the reverse domain. This is a typical distribution of antiphase boundaries in crystals cooled through T_c when very little domain wall movement occurs (Barkley and Jeitschko, 1973).

domain walls, our own work (unpublished) shows that E_0 is significantly increased by factors of 1.5 to 3, as a wall attempts to move through an array of these defects. Kumada (1973) uses deliberately induced defects to provide a well-defined threshold field which is advantageous in certain device applications.

Antiphase boundries have been observed in the β' phase by several methods. Barkley and Jeitschko (1973) found that dilute HCl (~5%) formed trench-like etch pits along antiphase boundries, as shown in fig. 30.31. These boundries were rearranged, annihilated and created by domain wall movement or by heating above the Curie temperature. Other researchers have also seen these boundries (Bohm and Kursten, 1973; Meleshina et al., 1974; Capelle and Malgrange, 1973; Yamaoto et al., 1974) with etching and/or X-ray topography or electron microscopy techniques.

The β'-$R_2(MoO_4)_3$ compositions have been and probably will continue to be a rich source of interesting phenomena related to coupled electrical, elastic and optical properties, which are fortutiously available at room temperature or above in high quality crystals readily grown.

References

Abrahams, S.C. and J.L. Bernstein, 1966, J. Chem. Phys. **45**, 2745.
Abrahams, S.C. and E.T. Keve, 1971a, Ferroelectrics **2**, No. 2, 129.
Abrahams, S.C., 1971b, Mat. Res. Bull. **6**, No. 10, 831.
Aizu, K., 1969, J. Phys. Soc. Jap. **27**, No. 2, 387.
Aizu, K., A. Kumada, H. Yumoto and S. Ashida, 1969, J. Phys. Soc. Jap. **27**, 511.
Aizu, K., 1971a, J. Phys. Soc. Jap. **31**, No. 3, 802.
Aizu, K., 1971b, J. Phys. Chem. Solids **32**, 1959.
Aizu, K., 1974, J. Phys. Soc. Jap. **36**, 1273.
Axe, J.D. and G. Shirane, 1970, Phys. Rev. **B1**, 342.
Axe, J.D., B. Dorner, and G. Shirane, 1971, Phys. Rev. Lett. **26**, 519.
Bagdasarov, Kh.S., G.A. Bogomolova, A.A. Kaminskii, A.M. Prokhorov, and T.M. Prokhortseva, 1971, Sov. Phys. – Doklady **16**, No. 3, 216.
Banks, E. and M. Nemiroff, 1974, Inorg. Chem. **13**, 2715.
Barkley, J.R., L.H. Brixner, E.M. Hogan, and R.K. Waring, Jr., 1972, Ferroelectrics **3**, 191.
Barkley, J.R. and W. Jeitschko, 1973, J. Appl. Phys., **44**, 938.
Blasse, G., 1966, J. Inorg. Nucl. Chem. **28**, 1488.
Bohm, J. and H.D. Kürsten, 1973, Phys. Status Solidi (a) **19**, 179.
Borchardt, H.J., 1965, J. Chem. Phys. **42**, No. 11, 3743.
Borchardt, H.J., P.E. Bierstedt, 1966, Appl. Phys. Lett. **8**, No. 2, 50.
Borchardt, H.J. and P.E. Bierstedt, 1967, J. Appl. Phys. **38**, No. 5, 2057.
Borchardt, H.J., 1968, Abstract No. 105, p. 265, Electrochem. Soc. Spring Meeting, Boston.
Bornarel, J., 1975, Ferroelectrics **9**, 197.
Boyer, L.L. and J.R. Hardy, 1972, Solid State Commun. **11**, 555.
Boyer, L.L. and J.R. Hardy, 1973, Phys. Rev. **B8**, 2205.
Brixner L.H., 1964, Inorg. Chem. **3**, 1065.
Brixner, L.H. and E. Abramson, 1965, J. Electrochem. Soc. **112**, 70.
Brixner, L.H., P.E. Bierstedt and A.W. Sleight, 1971, Mat. Res. Bull. **6**, 545.
Brixner, L.H., 1972, Mater. Res. Bull. **7**, 879.
Brixner, L.H., A.W. Sleight and M.S. Licis, 1972, J. Solid State Chem. **5**, 186.
Brixner, L.H., 1973, Rev. Chim. Minera. **10**, 47.
Brodale, G.E., R.A. Fisher, E.W. Hornung and W.F. Giauque, 1972, J. Chem. Phys. **56**, 6118.
Capelle, B. and C. Malgrange, 1973, Phys. Status Solidi (a) **20**, K5.
Cheung, K.M. and F.G. Ullman, 1974, Phys. Rev. **B10**, No. 11, 4760.
Chizhikov, S.I., N.G. Sorokin, B.I. Ostrovskii and V.A. Meleshina, 1971, Sov. Phys.-JETP Lett. **14**, 336.
Cleve, A., 1902, Z. anorg. allgem. Chem. **32**, 129.
Cohen, M.H., 1951, Phys. Rev. **84**, 369.
Courdille, J.M. and J. Dumas, 1973, Phys. Rev. **B8**, No. 8, 1129.
Courdille, J.M., R. Deroche and J. Dumas, 1975, J. Phys. (Paris) **36**, 891.
Craig, D.C. and N.C. Stephenson, 1968, Acta Crystallogr. **B24**, 1250.
Cross, L.E., A. Fousková and S.E. Cummins, 1968, Phys. Rev. Lett. **21**, No. 12, 812.
Cummins, S.E., 1970, Ferroelectrics **1**, 11.
Dem'yanov, V.V. and M.I. Shchedrin, 1973, Sov. Phys.-Solid State **14**, No. 10, 2620.

Dorner, B., J.D. Axe and G. Shirane, 1972, Phys. Rev. **B6**, No. 5, 1950.
Dvorak, V., 1971, Phys. Status Solidi (b) **46**, 763.
Elzen, van den, A.F. and G.D. Rieck, 1973, Acta Crystallogr. **B29**, 2436.
Epstein, D.J., W.V. Herrick and R.F. Turek, 1970, Solid State Commun. **8**, 1491.
Epstein, D.J., 1970, Technical Report AFAL-TR-70-172.
Esayan, S. Kh., Kh. S. Bagdasarov, V.V. Lemanov, T.M. Polkhovskaya and L.A. Shuvalov, 1974, Sov. Phys.-Solid State **16**, No. 1, 85.
Fisher, R.A., E.W. Hornung, G.E. Brodale and W.F. Giauque, 1972, J. Chem. Phys. **56**, 193.
Fisher, R.A., E.W. Hornung, G.E. Brodale and W.F. Giauque, 1973, J. Chem. Phys. **59**, 5798.
Fisher, R.A., E.W. Hornung, G.E. Brodale and W.F. Giauque, 1975, J. Chem. Phys. **63**, 1295.
Fleury, P.A., 1970, Solid State Commun. **8**, 601.
Fleury, P.A., 1971, Acoust. Soc. Amer. **49**, No. 3, 1041.
Flippen, R.B., 1975, J. Appl. Phys. **46**, No. 3, 1068.
Flippen, R.B. and C.W. Haas, 1973, Solid State Commun. **13**, 1207.
Fousek, J. and C. Konak, 1972, Czechoslovak J. Phys. **B22**, 995.
Fousková, A., 1969, J. Phys. Soc. Jap. **27**, 1699.
Frost, H.J. and M.F. Ashby, 1971, J. Appl. Phys. **42**, No. 13, 5273.
Ganguly, B.N., F.G. Ullman, R.D. Kirby and J.R. Hardy, 1975, Solid State Commun. **17**, 533.
Haas, C.W. and W.F. Jaep, 1974, Phys. Lett. **49A**, No. 1, 77.
Hitchcock, F.R.M., 1895, J. Amer. Chem. Soc. **17**, 522.
Höchli, U.T., 1972, Phys. Rev. **B6**, No. 5, 1814.
Hornung, E.W., G.E. Brodale, R.A. Fisher and W.F. Giauque, 1972, J. Chem. Phys. **56**, 5007.
Hubert, P.H., 1975, Bull. Soc. Chim. Fr. p. 161.
Janovec, V., 1976, Ferroelectrics **12**, 43.
Jeitschko, W., 1970, Naturwiss. **57**, 544.
Jeitschko, W., 1972, Acta Crystallogr. **B28**, 60.
Jeitschko, W., 1973, Acta Crystallogr. **B29**, 2074.
Jeitschko, W. and H. Wondratschek, 1974, Fortsch. Mineral. **52**, Beiheft 2, 30.
Kashiwada, Y. and S. Kishino, 1974, Jap. J. Appl. Phys. **13**, No. 2, 223.
Keller, C., 1962, Z. anorg. allgem. Chem. **318**, 89.
Keve, E.T., S.C. Abrahams, K. Nassau and A.M. Glass, 1970, Solid State Commun. **8**, 1517.
Keve, E.T., S.C. Abrahams and J.L. Bernstein, 1971, J. Chem. Phys. **54**, 3185.
Kittel, C., 1972, Solid State Commun. **10**, 119.
Klevtsova, R.F., V.A. Vinokurov and P.V. Klevtsov, 1972, Sov. Phys.-Crystallogr. **17**, 240.
Klevtsov, P.V., L.P. Kozeeva, V.I. Protasova, L. Yu. Kharchenko, L.A. Glinskaya, R.F. Klevtsova and V.V. Bakakin 1975, Sov. Phys.-Crystallogr. **20**, 31.
Kobayashi, J., Y. Sato and T. Nakamura, 1972, Phys. Status Solidi (a) **14**, 259.
Kumada, A., 1969, Phys. Letters **30A**, No. 3, 186.
Kumada, A., 1970, J. Jap. Soc. Appl. Phys. Suppl. **39**, 258.
Kumada, A., 1972, Ferroelectrics **3**, 115.
Kumada, A., 1973a, J. Phys. Soc. Jap. **35**, 941.
Kumada, A., 1973b, IEEE Trans. Electr. Devices **ED-20**, No. 10, 866.
Kumada, A., 1974, Ferroelectrics **7**, 145.
Kursten, H.D., J. Bohm, C. Scheiding and H. Blumberg, 1973, Kristall und Technik **8**, 303.
Levanyuk, A.P. and D.G. Sannikov, 1970, Fiz. Tverd. Tela. **12**, 2997.
McCarthy, G.J., 1971, Mater. Res. Bull. **6**, 31.
McCarthy, G.J., 1974, private communication to Megumi et al.
Megumi, K., H. Yumoto, S. Ashida, S. Akiyama and Y. Furuhata, 1974, Mat. Res. Bull. **9**, 391.
Meleshina, V.A., V.I. Indenbom, Kh. S. Bagdasarov and T.M. Polkhovskaya, 1974, Sov. Phys. Crystallogr. **18**, No. 6, 764.
Midorikawa, M., Y. Ishibashi and Y. Takagi, 1974, J. Phys. Soc. Jap. **37**, No. 6, 1583.
Miller, R.C., W.A. Nordland and K. Nassau, 1971, Ferroelectrics **2**, 97.
Nakamura, T., T. Kondo and A. Kumada, 1971a, Phys. Lett. **36A**, No. 2, 141.
Nakamura, T., T. Kondo and A. Kumada, 1971b, Solid State Commun. **9**, 2265.
Nassau, K., H.J. Levinstein and G.M. Loiacono, 1965, J. Phys. Chem. Solids **26**, 1805.
Nassau, K., J.W. Shiever and E.T. Keve, 1971, J. Solid State Chem. **3**, 411.
Newnham, R.E., H.A. McKinstry, C.W. Gregg and W.R. Stitt, 1969, Phys. Status Solidi **32**, K49.
Newnham, R.E., C.S. Miller, L.E. Cross, T.W. Cline, 1975, Phys. Status Solidi (a) **32**(1), 69.
Petzelt, J., 1971a, Solid State Commun. **9**, 1485.
Petzelt, J. and V. Dvorak, 1971b, Phys. Status Solidi (b) **46**, 413.
Pytte, E., 1970, Solid State Commun. **8**, 2101.
Sapriel, J., 1975, Phys. Rev. **B12**, 5128.
Sawaguchi, E. and L.E. Cross, 1973, J. Appl. Phys. **44**, No. 6, 2541.
Scheiding, C., G. Schmidt and H.D. Kürsten, 1973, Krist. Tech. **8**, 311.
Scott, J.F., 1974, Rev. Mod. Phys. **46**, No. 1, 83.
Shannon, R.D. and C.T. Prewitt, 1969, Acta Crystallogr. **B25**, 925.
Shepherd, I., 1971, Solid State Commun. **9**, 1857.
Shepherd, I. and J.R. Barkley, 1972, Solid State Commun. **10**, 123.
Shirokov, A.M., V.P. Mylov, A.I. Baranov and T.M. Prokhortseva, 1972, Sov. Phys.–Solid State **13**, No. 10, 2610.
Sillén, L.G. and K. Lundborg, 1943, Z. anorg. allgem. Chem. **252**, 2.
Smith, A.W. and G. Burns, 1969, Phys. Lett. **28A**, No. 7, 501.

Suzuki, K., 1972, Solid State Commun. **11**, 937.
Templeton, D.H. and A. Zalkin, 1963, Acta Crystallogr. **16**, 762.
Toledano, J.C., 1974, Ann. des Tekcommunications **29**, No. 7/8, 249.
Ullman, F.G., B.N. Ganguly and J.R. Zeidler, 1972, J. Electronic Materials **1**, No. 3, 425.
Ullman, F.G., K.M. Cheung, G.A. Rakes and B.N. Ganguly, 1975, Ferroelectrics **9**, 63.
Whinfrey C.G., D.W. Eckart and A. Tauber, 1960, J. Amer. Chem. Soc. **82**, 2695.
Wolfe, R.W. and R.E. Newnham, 1969, Solid State Commun. **7**, 1797.
Wondratschek, H. and W. Jeitschko, 1976, Acta Crystallogr. **A32**, 664.
Yamamoto, N., K. Yagi and G. Honjo, 1974, Phil. Mag. **30**, (5), 1161.
Zemann, J., 1956, Heidelb. Beitr. Mineral. Petrogr. **5**, 139.

lines, the temperature rise would increase the population of the more highly excited states and thus increase the intensity of transitions from these states relative to the intensity of the resonance radiation. As mentioned above, this is contrary to observations.

b. It is obvious that Doppler broadening at the existing temperatures is several orders of magnitude smaller than that shown in Fig. 4. Using conventional notation, the standard formula for collision broadening is (4)

$$\Delta\lambda/\lambda = N'd^2\lambda\sqrt{(3kT/4Mc^2)} \quad [1]$$

where $\Delta\lambda$ is the width of the line at half the intensity of the maximum, N' the number of atoms per unit volume, and d the effective diameter for a collision sufficiently close to affect the radiation process. To get this formula to agree with experiment, we must postulate a value for d some thirty times larger than its value obtained from kinetic theory. While results of this nature have been observed previously (5, 6), it should be emphasized that in our experiments the large increase in collision cross section occurs only under microwave action. The narrow width of the reversed lines indicates that whatever "perturbation" takes place, it affects solely the excited state.

Comparison with Other High Intensity Sources

In order to evaluate the usefulness of the microwave enhanced plasma source for practical applications, it is necessary to compare it with conventional high brightness sources, such as the Hanovia short arc xenon lamps. The performance of these conventional lamps is usually measured in terms of their luminous flux or their intensity. Since we measured the output of our enhanced sodium flame in terms of its brightness, it is necessary to correlate the two sets of parameters. For this purpose we use the expressions

$$B = 929L/4A, L/4\pi = C \quad [2]$$

where A is the source area in cm^2, B the brightness in ft-L, C the intensity in candles, and L the luminous flux in lumens. Strictly speaking, the relations in Eq. [2] are applicable only to sources radiating uniformly over a sphere. However, they should provide at least a good estimate of data for the sodium flame. The results of this comparison are listed in Table I. The value listed for the total power input into the enhanced flame is the sum of the thermal power input of 2.2 kw into the flame and the electrical power input of 2 kw into the magnetron. It is seen from the table that even for this total power input the efficiency of the enhanced sodium flame is far higher than that of either of the xenon lamps. Allowing for the fact that the coupling between the microwave field and the flame is only 25%, but with proper design can be made 90%, we can place the effective power input at only about 2.7 kw. The efficiency of the energy transformation is therefore as high as 220 lumens/w. Furthermore, since the enhanced sodium flame emits primarily in the region of the D-lines, it constitutes a source with the highest number of lumens per watt per angstrom. It has the additional attractive feature that it is capable of being pulsed to fit any desired pulse pattern.

Table I. Comparison of data for sodium flame

	Na flame	Xe arc, Lamp 1	Xe arc, Lamp 2
Power consumption (watts)	4,200	2,200	5,000
Luminous flux (lumens)	600,000	66,000	200,000
Intensity (candles)	50,000	5,300*	21,500
Efficiency (lumens/watt)	140	30	40

* Calculated from manufacturer's data using formula in Eq. [2].

Practical Considerations

No matter how efficient a lamp, it is not suitable for practical applications if it requires auxiliary gas tanks or a vacuum arrangement. We have therefore started work on simulating a flame by a completely self-contained system. The resonating cavity and the plasma enclosure are also in the process of being redesigned to provide more efficient coupling and to permit eliminating the tuning mechanisms.

Manuscript received July 8, 1964. This paper was presented at the Toronto Meeting, May 4-7, 1964.

Any discussion of this paper will appear in Discussion Section to be published in the December 1965 JOURNAL.

REFERENCES

1. J. A. Stratton, "Electromagnetic Theory," p. 490 ff, McGraw-Hill Book Co., New York (1941).
2. R. A. Kraushaar and A. Crivello, Private communication.
3. N. A. Lange, "Handbook of Chemistry," 10th Ed., p. 825, McGraw-Hill Book Co., New York (1961).
4. G. P. Harnwell and W. E. Stephens, "Atomic Physics," p. 110, McGraw-Hill Book Co., New York (1955).
5. H. E. White, "Introduction to Atomic Spectra," p. 430, McGraw-Hill Book Co., New York (1934).
6. R. W. Wood, "Physical Optics," 3rd Ed., p. 528, Macmillan Co., New York (1934).

On the Luminescent Properties of the Rare Earth Vanadates

L. H. Brixner and E. Abramson

Pigments Department and Central Research Department, respectively, E. I. du Pont de Nemours and Company, Inc., Wilmington, Delaware

ABSTRACT

X-ray examination of several Ln_2O_3/V_2O_5 systems indicated that compounds of the $LnVO_4$ type are the only ones formed by the rare earth sesquioxides and vanadium pentoxide. On the basis of this finding, we developed a flux-growing technique employing a V_2O_5 melt for the preparation of all rare earth vanadates in single crystalline form. With such monocrystals as well as with polycrystalline material we studied the fluorescent emission of the rare earth vanadates, and these data are reported and discussed.

The fact that YVO_4 crystallizes in the D_{4h}^{19}-I4/amd space group of zircon ($ZrSiO_4$) was first recognized by Broch (1), and since the ion radius of Y^{3+} is generally placed between Dy^{3+} and Ho^{3+} it was to be expected that at least some of the rare earth vanadates would crystallize in the same structure. Milligan, Watt, Rachford, and Vernon (2, 3) prepared all rare earth vanadates of the $LnVO_4$ type and found that with the exception of $LaVO_4$ they do indeed all crystallize in the $ZrSiO_4$ structure. Gambino and Guare (4) later con-

firmed these structures. Carron *et al.* (5) found that $LaVO_4$ has the monazite structure, which recently was confirmed by Schwarz (6) who conducted a comparative crystallographic study of all rare earth phosphates, arsenates, and vanadates.

The only information concerning the luminescent properties of the rare earth vanadates is given by Van Uitert (7) who investigated the $Y_{1-x}Eu_xVO_4$ system during a study on the role of f-orbital electron wave function mixing in the concentration quenching of Eu^{3+}. He used a $NaVO_3$ flux for the preparation of rare earth vanadates, but did not state anything about the size or quality of the obtained crystals. It still appeared desirable to look at the luminescent properties of all rare earth vanadates, particularly since the considerable thermal stability could make them excellent candidate materials for host lattices for optical maser materials if they can be grown in single crystal form by flame-fusion, Verneuil, or some other appropriate technique.

Experimental

All rare earth vanadates were prepared directly from high-purity V_2O_5 (obtained from the Vanadium Corporation of America), and the corresponding rare earth sesquioxides were obtained in 99.9% purity from the Lindsay Chemical Division of the American Potash and Chemical Corporation. Reaction was generally effected in two steps: first the stoichiometrically mixed powders of —200 mesh particle size were prereacted at 680°C (just below the melting point of V_2O_5) for some 10-14 hr. This reaction product was then ball-milled in a mechanical agate ballmill under acetone, dried, pressed into a 1-in. diameter pellet, and fired in a second step for some 10-14 hr at 1200°C. After this treatment, completely reacted, homogeneous materials were obtained, which failed to show any of the lines of the components upon x-ray examination. Weight losses for approximately 10g charges were generally below 0.1%. $CeVO_4$ and $PrVO_4$ were prepared under an inert atmosphere to avoid the possibility of oxidation of the trivalent rare earths to a higher valence state. Tb^{3+} in $TbVO_4$, which also forms higher oxides, did not show any tendency to oxidize and could be handled in air.

Small single crystals of all rare earth vanadates can be obtained from a V_2O_5 flux at 1000°C by simply charging a small quantity of any rare earth oxide (except Ce, Pr) into the V_2O_5 melt and letting it react for about 10-14 hr. Although crystals obtained in this fashion are rather small (up to 1 mm in cross section) they are of fair optical quality as an inspection under the microscope and in polarized light indicated. The major portion of the excess melt can be poured off while the remaining small quantity of V_2O_5 can be leached away with ammonia. Specifically for the systems Y_2O_3/V_2O_5 and Gd_2O_3/V_2O_5, we demonstrated that the $LnVO_4$ compound is the only existing phase by preparing eight different compositions of Ln_2O_3:V_2O_5 varying from 4:1 to 1:4. In each case, the $LnVO_4$ compound was the only new phase in addition to the excess component. Larger single crystals up to 1 cm long can be obtained by establishing a small temperature gradient in the flux and using a platinum wire seed, immersed about ¼ in. into the melt, as a "cold finger." Figures 1 and 2 show some single crystals of YVO_4 and $GdVO_4$, grown without seed in the above described way. Figure 3 gives a typical crystal cluster as obtained with the Pt seed.

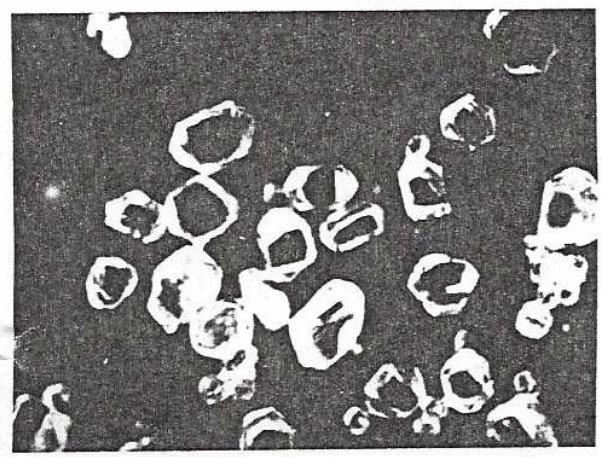

Fig. 1. Single crystals of $GdVO_4$. Magnification 10X

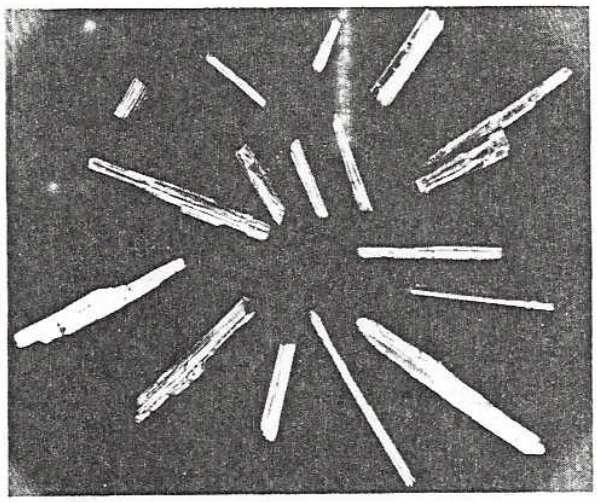

Fig. 2. Single crystals of YVO_4. Magnification approximately 7X

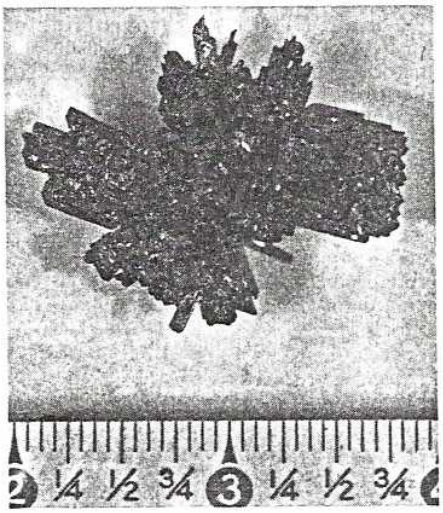

Fig. 3. Single crystal cluster of $GdVO_4$ grown on Pt wire

X-ray powder diffraction patterns were taken with a Philips 114.6 mm diameter camera at 25°C. The samples were sealed in 0.2 mm diameter Lindemann glass capillaries and were exposed to the K_α radiation of copper ($\lambda = 1.5418$Å) for 2-6 hr. Accurate parameters were obtained by extrapolation according to Nelson (8). Lattice dimensions and space groups of single crystals were determined by the rotating-crystal technique.

Crystallographic and Luminescent Properties

The measured lattice parameters are summarized in Table I, the asterisk denoting values obtained from single crystals. These parameters are in good agreement with those reported by Schwarz (*loc. cit.*)

Fluorescent emission in the visible region was first observed qualitatively under excitation by a 2537Å or

Table I. Luminescent and crystallographic data of the rare earth vanadates

Compound	Intrinsic color	Color of fluorescent emission 300°K 2537Å	3000Å	77°K 2537Å	3660Å		
$ScVO_4$	Tan	S Orange	W Orange	S Green-yellow	S Yellow-green	6.78*	6.12
YVO_4	White	S Yellow	S Yellow	S Blue-white	M Yellow-white	7.12*	6.27
$LaVO_4$	White	M Purple	W Purple	S Orange-yellow	M Yellow	Not characterized	
$CeVO_4$	Green	—	—	—	—	7.412	6.488
$PrVO_4$	Green-yellow	—	—	—	—	7.364	6.461
$NdVO_4$	Light blue	—	—	—	—	7.333	6.492
$SmVO_4$	Yellow-white	—	—	—	—	7.265	6.388
$EuVO_4$	White	W Purple	W Purple	M Blue-white	M Red	7.229	6.374
$GdVO_4$	White	S Red	S Red	S White	M Creme	7.17*	6.32
$TbVO_4$	Yellow-white	—	—	—	—	7.143	6.320
$DyVO_4$	White	—	—	—	—	7.137	3.310
$HoVO_4$	Peach	—	—	—	—	7.119	6.288
$ErVO_4$	Pink	—	—	M Blue-white	M Yellow	7.093	6.277
$TmVO_4$	White	—	—	—	—	7.069	6.261
$YbVO_4$	White	—	—	—	—	7.051	6.239
$LuVO_4$	White	S Yellow-white	S Yellow-white	S Blue-white	M Yellow	7.02*	6.22

* The letters S, M, and W denote Strong, Medium, and Weak intensities.

3660Å u.v. mineral light. Coarse quantitative fluorescent scans were made with a Beckman DK2 recording spectrometer with a mercury and phosphor lamp F4T5/BL (General Electric Company designation) through a Schott UG-11 filter which cuts off above 4000Å. Thus, excitation was between 3000 and 4000Å. The detector used was a photomultiplier tube 1P28 (Radio Corporation of America). These observations are also summarized in Table I.

More refined spectra were taken with samples excited by a filtered AH-3 mercury discharge lamp (primarily 3660Å radiation) with a Leeds and Northrup 0.5 meter Ebert mount grating spectrometer using again a 1P28 photomultiplier detector. Representative spectra of YVO_4 and $GdVO_4$ are shown in Fig. 4 and 5, and the characteristic fluorescent wavelengths of all the compounds so examined are summarized in Table II. The numbers in parentheses on the spectra give the relative intensity of the lines after correction for the spectral response of the detector.

The excitation spectrum (fluorescence intensity as a function of exciting wavelength) of $GdVO_4$, shown in Fig. 6, indicates that the principal excitation of this material occurred in a strong band whose half-maximum points are at 2500 and 3250Å. Since Gd^{3+} does not have strong, broad absorption bands in this wavelength region, the excitation of fluorescence must involve the VO_4^{3-} complex. This same absorption band must exist in all of the rare earth vanadates and be responsible for the major portion of their excitation.

Reference to Fig. 4 and 5 and to Table II shows that a number of the observed fluorescence multiplets, namely those centered about 4800, 5250, 5550, and 5750Å, are common to many of the compounds which emitted visible light. These multiplets may be due to the presence of rare earth impurities. In particular, the emission at 4800 and 5750Å could be ascribed to Dy^{3+} and that at 5450Å to Tb^{3+}. Although the two remaining multiplets at 5250 and 5550Å do not closely match known fluorescent transitions in any of the trivalent rare earth ions, it is possible that they are due, respectively, to Pr^{3+} and Er^{3+} impurities. That the muliplets may be inherent to the vanadate compound cannot, however, be completely ruled out except by the investigation of compounds prepared with controlled dopings of trivalent rare earth ions. This has been done only in the case of Eu^{3+} as an impurity.

Table II. Emission wavelengths of visibly fluorescing rare earth vanadates at room temperature

Compound	Emission wavelengths (Å)							
$ScVO_4$ No. 1	4800	5250		5460	5570	5750		
$ScVO_4$ No. 2	4800	5250		5460	5570	5750	5950[c]	6180[c]
YVO_4	4800[a]	5250		5460	5540	5750		
$GdVO_4$	4800[a]	5250	5380[c]	5460	5540	5750	5950[c]	6175[c]
$LaVO_4$	4800[b]						5950[c]	6175[c]
$EuVO_4$	4750	(low resolution spectrum)					5950	6180

[a] Plus weak broad band centered at 4750Å.
[b] Plus strong broad band centered at 4750Å.
[c] These lines due to Eu^{3+} contamination.

Although Tm^{3+} has energy levels at a separation corresponding to 4750Å, the 4f-4f transitions of trivalent rare earth ions are not known to occur in other than relatively sharp line multiplets. Hence, the broad band generally observed at 4750Å probably arises from

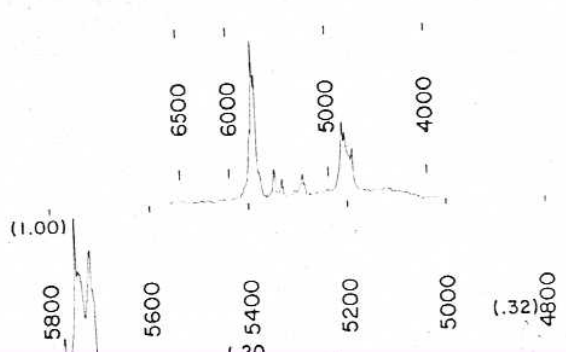

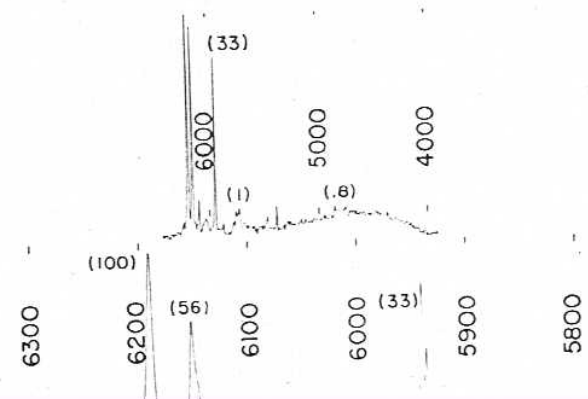

anionic group of the material or by a "charge transfer" transition involving the rare earth ion and a neighboring oxygen. With the present data, no choice between these two possibilities can be made. Excitation is then transferred predominantly to the lowest energy fluorescent levels, from which emission occurs. If the fluorescent energy levels of the principal rare-earth ion lie lower than those of the vanadate ion, most of the excitation energy is transferred to the rare-earth ion, which then emits its characteristic spectrum provided that concentration quenching is not too severe. $EuVO_4$ is an example of this process. If rare-earth ions with levels lower than those of the principal rare earth ion are present as dilute impurities in a host of the YVO_4 type, only a portion of the energy will be transferred to the lowest energy level as exemplified by the $Eu_xGd_{1-x}VO_4$ series. The broad fluorescence band generally evident at 4750Å may be due to a Stokes-shifted transition from the absorbing level to the ground state. The relative intensity of such a band would depend on the ratio between its transition probability and the probability of energy transfer to rare earth ions.

Acknowledgment

The authors would like to thank Dr. G. Teufer of the Engineering Research Laboratory for obtaining single crystal data and Mr. A. T. Weinmann for his assistance in obtaining powder data. We are also grateful to Messrs. L. S. Brooks and J. S. Ariganello for running the fluorescent emission spectra and to Mr. F. Y. Tse for taking the excitation spectra.

Manuscript received July 8, 1964.

Any discussion of this paper will appear in a Discussion Section to be published in the December 1965 JOURNAL.

REFERENCES

1. E. Broch, *Z. Phys. Chem.*, **20**, 345 (1933).
2. W. O. Milligan and L. W. Vernon, *J. Phys. Chem.*, **56**, 145 (1952).
3. W. O. Milligan, L. M. Watt, and H. J. Rachford, *J. Phys. and Colloid Chem.*, **53**, 227 (1949).
4. J. R. Gambino and C. J. Guare, *Nature*, **198**, 1084 (1963).
5. M. K. Carron, M. E. Mrose, and K. J. Murata, *Am. Mineral.*, **43**, 985 (1958).
6. H. Schwarz, *Z. anorg. allgem. Chem.*, **323**, 44 (1963).
7. L. G. van Uitert, R. C. Linares, R. R. Soden, and A. A. Ballman, *J. Chem. Phys.*, **36**, 702 (1962).
8. J. B. Nelson and D. P. Riley, *Proc. Phys. Soc.*, **57**, 160 (1945).
9. L. G. DeShazer and G. H. Dieke, *J. Chem. Phys.*, **38**, 2190 (1963).
10. R. E. MacDonald, M. J. Vogee, and J. W. Brookmann, *IBM J. of Res. and Dev.*, **6**, 363 (1962).
11. L. H. Brixner, *This Journal*, **111**, 693 (1964).
12. F. A. Kröger, "Some Aspects of the Luminescence of Solids," p. 95, Elsevier Publishing Co., Inc. (1948).
13. L. G. van Uitert and R. R. Soden, *J. Chem. Phys.*, **32**, 1687 (1960).
14. H. Witzmann, K. Th. Wilke, J. Buhrow, and H. J. Bohm, *Z. Phys. Chem.*, **222**, 271 (1963).
15. L. H. Brixner, *This Journal*, To be published.
16. H. Borchardt, *J. Chem. Phys.*, To be published.
17. H. J. Borchardt, *ibid.*, **39**, 504 (1963).

Chemical and Optical Studies of Samarium Doped CaF_2 Type Single Crystals

P. F. Weller, J. D. Axe*, and G. D. Pettit

Thomas J. Watson Research Center, International Business Machines Corporation, Yorktown Heights, New York

ABSTRACT

Single crystals of CaF_2 and $Ca_{1-x}Sr_xF_2$ were grown by the Czochralski technique and doped with varying concentrations of samarium. Complete solid solution was found in the CaF_2-SrF_2 pseudobinary system with a minimum near 50% CaF_2 at 1330° ± 10°C. The concentration of Sm^{+2} depended on the melt concentrations of SmF_3 and Sm metal, and the samarium segregation coefficient did not change significantly with samarium concentration. The fluorescence efficiency of Sm^{+2} as a function of Sm^{+2} concentration appeared to go to a broad maximum at about 0.1% Sm^{+2}. The fluorescent emission in $Ca_{1-x}Sr_xF_2$:Sm^{+2} showed pronounced inhomogeneous line broadening.

The discovery of a CaF_2:Sm^{+2} laser (1) stimulated interest in the CaF_2-Sm system. In order to optimize laser efficiency, it seemed necessary to obtain more perfect crystals with better control of the doping levels, oxidation state ratios, and homogeneity. We have used the Czochralski technique to grow samarium doped CaF_2 and $Ca_{1-x}Sr_xF_2$ crystals (2). Crystal perfection has been indicated by the number of imperfections appearing as voids and growth "streamers," the number of dislocations, and the amount of light scattering that occurred in the crystals. Oxidation state variations were achieved by varying the amount of reducing agent, samarium metal, added to the sample charge. Doping homogeneity was improved considerably by a samarium segregation coefficient near unity which was essentially concentration independent over the range studied. However, crystal growth parameters such as the ratios of crystal diameter to crucible diameter and melt surface to melt volume did affect Sm^{+2} homogeneity considerably. Optimum Sm^{+2} doping levels for maximum fluorescence efficiency were indicated by studying the efficiency as a function of Sm^{+2} concentration. The strong effect of certain impurities on the Sm^{+2} fluorescence was shown by the severe line broadening in the $Ca_{1-x}Sr_xF_2$:Sm^{+2} fluorescence experiments.

* This research has been supported in part by the Army Research Office, Durham, North Carolina.

Crystal Growth

Starting materials.—CaF_2 was obtained from the Harshaw Chemical Company as random cut chips (highest quality). SrF_2 was prepared synthetically using a flux method (3).

$$SrCl_2 + 2KF \rightarrow SrF_2 + 2KCl \quad [1]$$

The SrF_2 was then carefully fired in flowing HF gas at about 1300°C for several hours or crystallized using a Bridgman-Stockbarger technique with a PbF_2 oxygen "scavenger" added (4).

Samarium trifluoride and metal were obtained from the Lindsay Division of American Potash and Chemical Company. SmF_3 was HF fired at about 1200°C, and the samarium metal was H_2 fired at about 1000°C.

Growth procedure.—The crystals were grown in an apparatus described previously (5). Graphite, platinum, and molybdenum crucibles were used with molybdenum being most satisfactory. A graphite sus-